Influence of the variable inertia rotational mechanism on natural frequency and structural response

Anika T. Sarkar[1] and Nicholas E. Wierschem[2*]

[1,2] *Department of Civil and Environmental Engineering, The University of Tennessee*
325 John D. Tickle Engineering Building, 851 Neyland Drive, Knoxville TN 37996-2313, U.S.A.

(Received , Revised , Accepted)

Abstract. Rotational inertial mechanisms (RIMs) are promising for structural control as their mass amplification properties allow them to impart large mass effects. While most research on RIMs involves the linear inerter, there is interest in utilizing the variable mass effects from nonlinear RIMs (NRIMs). One type of NRIM is the variable inertia rotational mechanism (VIRM), which features moving masses in the device's flywheel that alter the flywheel's rotational inertia. While active and semi-active forms of the VIRM were previously considered, few studies have considered the passive VIRM. Consequently, the effect of VIRM parameters, the VIRM's capacity for shifting natural frequencies, and the performance of the VIRM under various loading types remain uncertain. This paper investigates the VIRM when attached to a single-degree-of-freedom primary structure. A mathematical model is derived for the combined primary structure and VIRM. Numerical simulations are carried out to determine the effect of the VIRM on the system's natural frequencies and dynamic response. This study demonstrates that the VIRM can significantly shift the primary structure's instantaneous and pseudo-natural frequencies, add higher frequency dynamics, and reduce the response of the structure in many cases, but that the impact of the VIRM is highly dependent on load type and amplitude.

Keywords: Variable inertia rotational mechanism, Nonlinear, Inerter, Natural Frequency

1 Introduction

Excessive vibration in civil engineering structures can cause human discomfort, fatigue, damage, and even the collapse of the structure; thus, vibration control is critical in many structures. In recent years, rotational inertial mechanisms, most prominently the inerter, have attracted attention in academia and industry as a potential part of passive vibration control systems. The term 'inerter' was proposed by Smith in the context of the force-current analogy between electrical and mechanical networks (Smith 2002). The inerter is a two-terminal mechanical element that can be realized with various physical means, e.g., the ball-screw assembly, rack-and-pinion, and fluid-based mechanisms (Smith 2002, 2008, 2012; Swift et al. 2013). The inerter generates force proportional to the relative acceleration across its two terminals, and the constant of proportionality is known as 'inertance', which has the same units as mass. The inerter can produce a mass amplification effect by transforming translational motion into the rotational motion of a flywheel. Hence, the inerter has been applied to a number of novel vibration control systems as well as to reduce the mass of modified conventional vibration control systems. Examples of inerter-based vibration control devices include the tuned-mass-damper-inerter, rotational inertia double-tuned mass damper, rotational inertia viscous damper, inertia mass damper with an electromagnetic damper, friction pendulum inerter system, and inerters combined with an external rocking wall of a frame system (Di Egidio et al. 2021; Giaralis and Petrini 2017; Huang et al. 2019; Hwang et al. 2007; Jangid 2022; Javidialesaadi and Wierschem 2019; Marian, Laurentiu and Giaralis, Agathoklis 2017; Nakamura et al. 2014; Wang et al. 2019; Zhao et al. 2019).

Most of the previously studied devices featuring rotational inertial components generate constant effective mass, whereas very few provide variable effective mass (Li et al. 2021b; Mahato et al. 2019; Xu et al. 2015; Zhang et al. 2020). Due to their constant effective mass, inerters can be described as linear rotational inertial mechanisms. However, as the research in this field progresses, there is growing interest in understanding the dynamics of nonlinear rotational inertial mechanisms that produce variable inertance. The inertance of such nonlinear rotational inertial mechanisms is not fixed; rather, the inertance can depend on factors related to the device's response, such as the relative displacement of the device and the rotational velocity of the device's flywheel. These nonlinear rotational inertial

[1] Ph.D. Student
Email: asarkar6@vols.utk.edu
[2] Ph.D.

[*] Corresponding author, Ph.D.
Email: nwiersch@utk.edu

mechanisms can be divided into categories including functionally varied inertance mechanisms ($b = f(u, \dot{u}, \ddot{u})$, where b is inertance that varies as a smooth function of u, $\dot{u}$, $\ddot{u}$, the displacement, velocity, or the acceleration of the structure) and state-switching mechanisms ($b=b_1$ if condition 1, $b=b_2$ if condition 2, and so on). While this study will consider a functionally varied inertance mechanism, an example of a state switching mechanism is found in the clutch-inerter damper. The clutch-inerter damper consists of two flywheels and a passive clutch system, which transforms translational motion into flywheel rotational motion and prevents the kinetic energy in the flywheel from transferring back to the structure (Javidialesaadi and Wierschem 2019; Makris and Kampas 2016; Makris and Moghimi 2019; Málaga-Chuquitaype et al. 2019; Talley et al. 2023; Wang and Sun 2018).

Functionally varied inertance mechanisms that have attracted much attention in recent years include a geometrically nonlinear inertance mechanism that has been used as a vibration isolator (Moraes et al. 2018; Yang et al. 2020). The geometrically nonlinear inertance mechanism features a pair of oblique inerters and the studies' results demonstrated that the geometrically nonlinear inertance mechanism possesses several performance benefits over conventional isolators, such as, improved higher frequency isolation and smaller displacement amplitude and force transmissibility, depending on the frequency range and amplitude of the excitation. Alternatively, other functionally varied inertance mechanisms have been developed by using a controller or a continuously variable transmission to adjust inertance in traditional tuned damper systems. Some examples of these are an adaptive tuned heave plate to mitigate heave motion of floating platforms (Ma et al. 2023), an adaptive tuned viscous inertance damper (Ali Sadeghian et al. 2021), and a tuned mass damper with changeable inertance (Brzeski et al. 2017).

In addition to these, another functionally varied inertance mechanism can be produced by modifying the rotational inertia of a device's flywheel (Dong et al. 2018; Jauch 2015; Kushwaha et al. 2020; Li et al. 2021a; Mahato et al. 2019; Xu et al. 2015; Zhang et al. 2020). Nonlinear rotational inertia from the variable moment of inertia of a flywheel can be obtained through flywheel designs that allow the distribution of mass to change during the response of the flywheel; for example, a flywheel with masses that can move within slots radially on the flywheel. These variable inertia rotational mechanisms (VIRM) have the potential to cause significant passive changes to the dynamics of the system they are attached to, which may be exploited as part of a vibration control strategy. However, the majority of VIRM research has been pursued through active or semi-active control methodologies that require input energy and intricate hardware. This includes work on a variable inertia flywheel (VIF) with energy storage and power control functionality, and VIF with magneto-rheological technology to adjust natural frequency and suppress the torsional vibration of a system (Dong et al. 2018; Li et al. 2021b; Ullman 1978; Yuan et al. 2010). In contrast to the above active and semi-active mechanisms, Xu and Yang proposed a VIF for a passive vehicle suspension system and showed improved rider comfort, better road handling and safety and reduced suspension deflection under most circumstances (Xu et al. 2015; Yang et al. 2019). Additionally, researchers have explored installing VIF in various rotary systems such as hydraulic motors, diesel generators, wave energy converters and wind turbine rotors. These studies aimed to enhance stability, increase power absorption bandwidth and enable passive vibration control of the systems (Jauch 2015; Kushwaha et al. 2020; Li et al. 2021a; Mahato et al. 2019; Yang et al. 2016).

Although research has been conducted on VIRMs to evaluate their effectiveness in reducing the response amplitude of dynamic systems, studies investigating passive VIRMs are rare. Furthermore, the existing limited research on passive VIRMs has predominantly concentrated on their application in rotating machinery systems, while their potential utilization in other types of mechanical or civil engineering structures has been unexplored. The majority of the prior investigations have primarily examined the VIRM's performance under sinusoidal or impulse loading conditions; thus, its behavior under random excitation scenarios remains unknown. As a result, there is a notable lack of understanding of the impact of variable rotational inertia on the natural frequency changes in the structure they are utilized in under different loading scenarios. While limited research exists in understanding the effect of constant rotational inertia on a system's natural frequencies (Chen et al. 2014), additional investigation is imperative to characterize the effect of variable rotational inertia on the natural frequency and the response of a structure equipped with a VIRM under external excitation. To address these gaps in knowledge, the main objective of this study is to numerically evaluate the effects of a passive VIRM on the natural frequency and response amplitude of a single-degree-of-freedom (SDOF) structure under different types of excitations.

In this study, a passive VIRM is considered in which multiple mass-spring-damper elements are symmetrically positioned on a circular flywheel, which is connected to a ball screw and attached to a SDOF structure. The vibration of the structure with the VIRM drives the ball screw and results in the rotation of the VIRM flywheel. Centrifugal force pushes the masses on the flywheel outward towards the boundary of the baseplate causing a dynamically changing inertia. In this numerical study, the VIRM is incorporated into a SDOF structure and numerical simulations are carried out given a collection of initial displacement conditions, harmonic loading, and white noise loading to investigate the evolution of the structure's frequencies during the response. The effects of the damper properties of the VIRM on the natural frequency shift, overall fundamental frequency, and the response reduction are also explored. Comparisons in this study are made with a fixed inertia rotational mechanism (FIRM).

The organization of this paper is as follows. In Section 2, the mechanism of the VIRM and a dynamic model of it installed in a SDOF structure are presented. The methodologies for determining relevant response measures, such as the instantaneous frequency, overall fundamental frequency, and an H_2 response measure, are described in

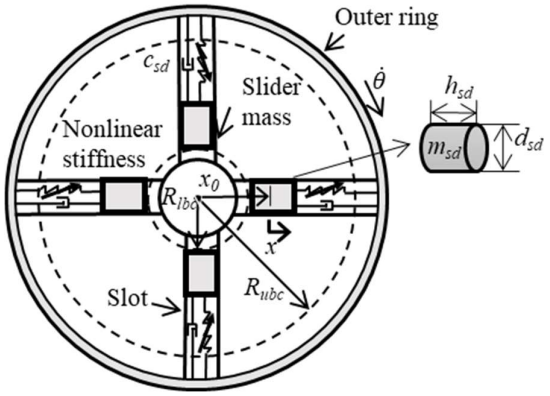

(a) Schematic diagram of the VIRM with slider masses shown located at their initial position

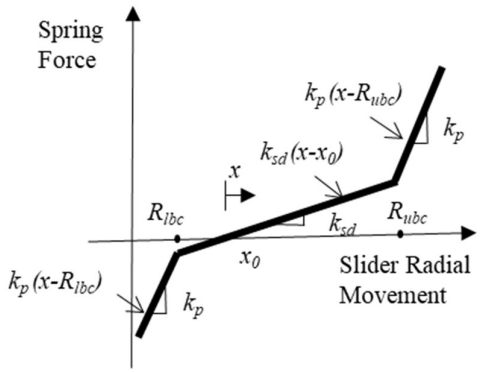

(b) Force-displacement relationship of the trilinear spring attached to the slider masses on the flywheel of the VIRM

Fig. 1 Characteristics of VIRM

Section 3. The effect of the VIRM on the instantaneous and overall fundamental frequencies are presented in Sections 4 and 0, respectively. The effectiveness of the device to reduce the structure's displacement response under different loads is discussed in Section 6. In Section 7, the contributions of this study are summarized and conclusions are drawn.

2 Variable inertia rotational mechanism

In this study, the variable inertance of the VIRM is produced by utilizing the flywheel rotational velocity to passively alter the arrangement of masses in the flywheel. A schematic diagram of the VIRM flywheel considered is presented in Fig. 1(a). This VIRM flywheel consists of a circular plate with four symmetrically spaced mass-spring-damper elements. These masses are constrained such that they can only move radially in the flywheel. When the flywheel is at rest, the springs attached to these masses are at their free length and the masses are located at an initial radial position near the center of the flywheel, x_0. As the absolute rotational velocity of the flywheel increases, the masses move, in general, radially outward from the center of the flywheel due to the increasing centrifugal force. When the absolute flywheel velocity decreases, the masses will slide back towards the center of the flywheel. The movement of these masses results in the variable moment of inertia of the flywheel. The viscous dampers (c_{sd}) in the VIRM flywheel damp the motion of these masses and dissipate energy in the system. The radial motion of the masses causes a restoring force in the springs that increases with the change in the radial position of the masses. The springs are assumed to have a trilinear elastic force-displacement relationship with a soft central spring k_{sd} and two equal, but much stiffer, penalty spring segments, as illustrated in Fig. 1(b). The relatively stiff penalty spring stiffness (k_p) in the VIRM is activated when the slider mass approaches the center or the upper bound contact point near the outer ring of the flywheel and works to restrain the movement of the slider mass. The position of the two locations on the radius where the penalty spring stiffness segments are engaged are called the lower bound contact point, R_{lbc} and upper bound contact point, R_{ubc}, respectively. Centrifugal force on the slider masses increases with larger flywheel rotational velocity and increased radial position of the masses; thus, the slider masses are expected to move significantly beyond R_{ubc} with increasing system excitation. However, due to the lower centrifugal forces near the center of the flywheel, the masses are not expected to go significantly beyond R_{lbc}.

Compared to a VIRM, all of the components of a FIRM are kept fixed in the same configuration regardless of the flywheel's rotational velocity. In this study, comparisons of the resulting dynamics and behavior of a system with a VIRM will be made to a system with a FIRM with its masses fixed in their initial position and with a FIRM with masses fixed at the R_{ubc} position.

The relationship between the flywheel angular velocity ($\dot{\theta}$) and the relative velocity ($\dot{u}$) of the structure between the attachment points of the VIRM or FIRM is as follows

$$\dot{\theta} = \alpha \dot{u} \tag{1}$$

where α is the coefficient governing this relationship. Utilizing a ball-screw, α is $2\pi/\rho$ where ρ is the lead of the ball-screw.

The total moment of inertia of the VIRM flywheel assembly can be expressed as

$$J_{VIRM} = \frac{1}{12} n m_{sd} \left(\frac{3}{4} {d_{sd}}^2 + {h_{sd}}^2 \right) + \frac{1}{2} m_c r^2 + n m_{sd} x^2 \tag{2}$$

where n, m_{sd}, d_{sd}, h_{sd}, m_c, and r are the number of slots, slider masses, slider diameter, height, mass of the flywheel without the sliders, and radius of the flywheel, respectively. Note that the total flywheel moment of inertia includes static components that are dependent on the flywheel mass and dimensions and a component that depends on the radial position of the slider masses. In Eq. (2), the last term ($nm_{sd}x^2$) is governed by the radial position (x) of the slider masses. The radial position is replaced with x_0 or R_{ubc} to determine the constant moment of inertia of the two FIRM flywheels. The inertance generated by the constant moment of inertia of the FIRM configuration is $b_y = \left((1/12) * n m_{sd} \left((3/4) * {d_{sd}}^2 + {h_{sd}}^2 \right) + (1/2) * m_c r^2 + n m_{sd} y^2 \right) \alpha^2$

for the FIRM with slider masses fixed at 'y' location. This study replaces the 'y' location with x_0 or R_{ubc}. The normalized inertance for the two FIRM configurations is expressed as

$$\lambda_{x_0} = \frac{b_{x_0}}{m_s},\ \lambda_{R_{\max}} = \frac{b_{R_{\max}}}{m_s} \tag{3}$$

Fig. 2 shows a model with a VIRM attached to a SDOF structure subjected to an external force, *P(t)*. In this figure, m_s represents the mass of the structure, k_s, and c_s are the stiffness and viscous damping coefficients of the structure. When the VIRM is replaced with a FIRM, the structure behaves like a typical spring-mass-damper-inerter (linear) structure and the inertance value provided to the structure is constant.

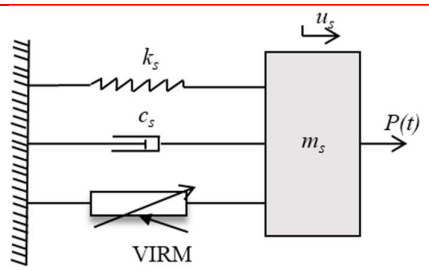

Fig. 2 SDOF primary structure with VIRM attached

The equation of motion of the system can be obtained using Lagrange's equation. The Lagrangian, L, is defined as

$$L = T - V \tag{4}$$

where T and V are the system's kinetic energy and potential energy, respectively. The kinetic energy of the system is calculated considering the motion of the structure, the rotational velocity of the flywheel, and the components of the slider mass velocity. The potential energy of the structure includes the energy stored in all the springs, this includes springs related to the structural stiffness (k_s) and the VIRM stiffness (k_{sd}, k_p). The effect of gravity is ignored here. The kinetic energy, potential energy, and the virtual work of non-conservative forces, ∂W_{NC}, can be formulated as

$$\begin{aligned}
T &= \frac{1}{2}m_s\dot{u}^2 + \frac{1}{2}\left(\frac{1}{12}nm_{sd}\left(\frac{3}{4}{d_{sd}}^2 + {h_{sd}}^2\right) + \frac{1}{2}m_c r^2\right)\alpha^2\dot{u}^2 \\
&+ n\frac{1}{2}m_{sd}\dot{x}^2 + n\frac{1}{2}m_{sd}x^2\alpha^2\dot{u}^2 \\
V &= \begin{cases}
\frac{1}{2}k_s u^2 + n\frac{1}{2}k_{sd}\left(R_{lbc} - x_0\right)^2 + n\frac{1}{2}k_p\left(x - R_{lbc}\right)^2 \\
\quad + nk_{sd}\left(R_{lbc} - x_0\right)\left(x - R_{lbc}\right), x < R_{lbc} \\
\frac{1}{2}k_s u^2 + n\frac{1}{2}k_{sd}\left(x - x_0\right)^2, R_{lbc} \le x < R_{ubc} \\
\frac{1}{2}k_s u^2 + n\frac{1}{2}k_{sd}\left(R_{ubc} - x_0\right)^2 + n\frac{1}{2}k_p\left(x - R_{ubc}\right)^2 \\
\quad + nk_{sd}\left(R_{ubc} - x_0\right)\left(x - R_{ubc}\right), x \ge R_{ubc}
\end{cases} \\
\partial W_{NC} &= \left(P(t) - c_s\dot{u}\right)\partial u - nc_{sd}\dot{x}\partial x
\end{aligned} \tag{5}$$

Note that in these equations the multiple slider masses in the VIRM are assumed to be moving synchronously with the same radial motion.

Lagrange's equation for the system in generalized coordinates is given as

$$\frac{d}{dt}\frac{\partial \mathrm{T}}{\partial \dot{q}_i} - \frac{\partial \mathrm{T}}{\partial q_i} + \frac{\partial V}{\partial q_i} = p_i(t),\ i = 1,2; \tag{6}$$

where q_1 is the displacement of the primary structure (u) and q_2 is the radial displacement of the slider mass (x). The resulting equations of motion can be expressed as

$$\begin{aligned}
&m_s\ddot{u} + \left(\frac{1}{12}nm_{sd}\left(\frac{3}{4}{d_{sd}}^2 + {h_{sd}}^2\right) + \frac{1}{2}m_c r^2\right)\alpha^2\ddot{u} \\
&+2nm_{sd}x\dot{x}\alpha^2\dot{u} + nm_{sd}x^2\alpha^2\ddot{u} + c_s\dot{u} + k_s u = P(t) \\
&m_{sd}\ddot{x} - m_{sd}x\alpha^2\dot{u}^2 + F_{bsd} + c_{sd}\dot{x} = 0
\end{aligned} \tag{7}$$

In the above equations, F_{bsd} represents the restoring force from the trilinear springs in the model. This restoring force varies depending on the radial position of the slider masses and can be defined as

$$\begin{aligned}
F_{bsd} &= k_{sd}\left(R_{lbc} - x_0\right) + k_p\left(x - R_{lbc}\right),\ x < R_{lbc} \\
F_{bsd} &= k_{sd}\left(x - x_0\right), R_{lbc} \le x < R_{ubc} \\
F_{bsd} &= k_{sd}\left(R_{ubc} - x_0\right) + k_p\left(x - R_{ubc}\right), x \ge R_{ubc}
\end{aligned} \tag{8}$$

In most previous work, the Coriolis force on the slider masses in the VIF was not accounted for (Xu et al. 2015; Yang et al. 2020; Zhang et al. 2020). For example, the kinetic energy generated from the tangential velocity component of the sliders are ignored. This study accounts for forces acting radially and tangentially to the direction of motion. Additionally, unlike most other work in this area, penalty springs that restrain the excessive motion of the slider masses are considered in this study (Dong et al. 2018; Xu et al. 2015; Yang et al. 2016).

For the FIRM, the slider mass springs and dampers are removed, and the slider masses are kept fixed with the flywheel frame at either x_0 or R_{ubc}, which results in the constant moment of inertia of the flywheel. The equation of motion of the primary structure with the FIRM is

$$\begin{aligned}
&m_s\ddot{u} + \left(\frac{1}{12}nm_{sd}\left(\frac{3}{4}{d_{sd}}^2 + {h_{sd}}^2\right) + \frac{1}{2}m_c r^2 + nm_{sd}y^2\right)\alpha^2\ddot{u} \\
&+c_s\dot{u} + k_s u = P(t)
\end{aligned} \tag{9}$$

In Eq. (9), the fixed position of the slider mass is denoted by y.

To facilitate a generalized analysis and comparison of system behavior across different physical parameters, Eq. (7), Eq. (8), and Eq. (9) are normalized. This normalization reduces the number of independent parameters and highlights the system's fundamental characteristics. The normalized system parameters are the slider mass ratio, flywheel mass ratio without sliders, frequency ratio, structure damping ratio, slider damping ratio, and stiffness ratio, which are defined in the next paragraph. Using the normalized parameters, Eq. (7), Eq. (8), and Eq. (9) can be rewritten as

$$U''+\left(\frac{1}{12}n\mu_1\left(\frac{3}{4}{d_{sd}}^2+{h_{sd}}^2\right)+\frac{1}{2}\mu_2 r^2\right)\alpha^2U''$$
$$+2n\mu_1\alpha^2\beta XX'U'+n\mu_1X^2\alpha^2U''+2\xi_sU'+U=F(t) \quad (10)$$
$$X''-X\frac{\alpha^2}{\beta}U'^2+F_B+2\xi_{sd}X'=0$$

$$F_B=R_{lbc}-x_0+\kappa(X-R_{lbc}),\ X<R_{lbc}$$
$$F_B=X-x_0,\ R_{lbc}\le X<R_{ubc} \quad (11)$$
$$F_B=R_{ubc}-x_0+\kappa(X-R_{ubc}),\ X\ge R_{ubc}$$

$$U''+\left(\frac{1}{12}n\mu_1\left(\frac{3}{4}{d_{sd}}^2+{h_{sd}}^2\right)+\frac{1}{2}\mu_2 r^2+n\mu_1Y^2\right)\alpha^2U''$$
$$+2\xi_sU'+U=F(t) \quad (12)$$

where $\mu_1=m_{sd}/m_s$: slider mass ratio;
$\mu_2=m_c/m_s$: flywheel mass ratio without slider masses;
$\omega_{s_0}=\sqrt{k_s/m_s}$: natural frequency of the primary structure without VIRM/FIRM;
$\omega_{sd}=\sqrt{k_{sd}/m_{sd}}$: linearized natural frequency of the slider mass; $\beta=\omega_{sd}/\omega_{s_0}$: frequency ratio;
$U=u$: displacement of the primary structure;
$U'=\dot{u}/\omega_{s_0}$: normalized velocity of the primary structure;
$U''=\ddot{u}/{\omega_{s_0}}^2$: normalized acceleration of the primary structure;
$X=x$: displacement of the slider;
$X'=\dot{x}/\omega_{sd}$: normalized velocity of the slider;
$X''=\ddot{x}/{\omega_{sd}}^2$: normalized acceleration of the slider;
$\xi_s=c_s/2m_s\omega_{s_0}$: primary structure damping ratio;
$\xi_{sd}=c_{sd}/2m_{sd}\omega_{sd}$: linearized damping ratio of the slider mass;
$\kappa=k_p/k_{sd}$: stiffness ratio;
$F(t)=P(t)/k_s$: normalized force amplitude;
F_B: normalized slider stiffness restoring force

While the normalization scheme reduces the number of independent parameters, note that it does not render all parameters dimensionless. For instance, the spatial dimensions, such as displacement, position, height and depth retain their dimensions. The original dimension of the displacement allows for a more intuitive understanding of the primary structure's movement (in 'm'), which is a key response considered in this study. Furthermore, the complexity of the system makes it challenging to achieve complete non-dimensionality. Velocity and acceleration, for example, are normalized by the natural frequency of the corresponding system. Similarly, the external forces (N) are normalized by the stiffness (N/m) of the primary structure, resulting in a unit of displacement ('m') for all load cases considered.

3 Numerical analysis and response measures

In this study, the response of the structure with the VIRM or the FIRM, presented by the equations of motion in Eq. (7) and Eq. (9), is simulated under different loadings using the MATLAB implicit solver (MathWorks 2022a) with an output frequency set at 4000 Hz. The loading considered in different parts of this study are harmonic excitations with different input frequencies, initial displacements, and white noise. The structure and VIRM parameters selected for these numerical simulations are shown in Table 1. While Table 1 provides a single value for the slider damping ratio, Sections 4, 5 and 6 will investigate its influence on system's dynamics across a range of values.

Table 1 Structure and VIRM parameters

Symbol	Description	Value
n	Slider number	4
μ_1	Slider mass ratio	0.0005
μ_2	Flywheel mass ratio (without sliders)	0.0017
ω_{s_0}	Primary structure natural frequency (without VIRM/FIRM)	2.91 Hz
ω_{sd}	Slider mass linearized natural frequency	42 Hz
β	Frequency ratio	14.64
ξ_s	Primary structure inherent damping ratio	0.02
ξ_{sd}	Linearized slider damping ratio	4
κ	Stiffness ratio	100
λ_{x_0}	Inertance ratio at initial position, x_0	0.086
$\lambda_{R_{ubc}}$	Inertance ratio at R_{ubc}	0.25
d_{sd}	Slider diameter	0.02 m
h_{sd}	Slider height	0.015 m
r	Radius of the flywheel	0.1 m
x_0	Initial radial position of the slider	0.01 m
α	Proportionality constant between the relative velocity of the structure and the angular velocity of the flywheel	100 rad/m
R_{ubc}	Radial position of the upper bound contact point of the penalty spring	0.095 m
R_{lbc}	Radial position of the lower bound contact point of the penalty spring	0.005 m

The parameters listed in Table 1 are selected based on the following considerations. The primary structure's natural frequency and the damping ratio are selected to represent typical values observed in civil structures, ensuring the relevance of the findings to real-world applications in structural vibration control. The proportionality constant governing the relationship between the structure's relative velocity and the flywheel's rotational velocity, along with the flywheel's inherent parameters, are specifically chosen to encompass a wide range of rotational inertia variability. This deliberate selection facilitates a thorough examination of the impact of the VIRM's dynamically changing inertia on the response of the primary structure.

To quantitatively evaluate the response of the dynamic systems studied, several measures are calculated from the system responses. These measures, which are described in detail below, include the instantaneous frequency (ω_{IF}), the

weighted average instantaneous frequency $(\bar{\omega}_w)$, the overall fundamental frequency (ω_0), and the H_2 norm analog (H_2). The ω_{IF}, $\bar{\omega}_w$, and ω_0 are normalized using the natural frequency of the structure without the VIRM or the FIRM, ω_{s_0}, which can be expressed as

$$\Psi_{\omega_{IF}} = \frac{\omega_{IF}}{\omega_{s_0}},\ \Psi_{\bar{\omega}_w} = \frac{\bar{\omega}_w}{\omega_{s_0}},\ \Psi_{\omega_0} = \frac{\omega_0}{\omega_{s_0}} \tag{13}$$

where $\Psi_{\omega_{IF}}$, $\Psi_{\bar{\omega}_w}$, and Ψ_{ω_0} are the normalized ω_{IF} ratio, normalized $\bar{\omega}_w$ ratio and normalized ω_0 ratio, respectively.

Additionally, the harmonic loading frequency (ω_l) and the response frequency (ω_r) considered in the study are also normalized by the natural frequency of the structure without the VIRM or the FIRM. These are expressed as

$$\Psi_l = \frac{\omega_l}{\omega_{s_0}},\ \Psi_r = \frac{\omega_r}{\omega_{s_0}} \tag{14}$$

where Ψ_l and Ψ_r are the loading frequency ratio and response frequency ratio, respectively.

3.1 Instantaneous frequency

The ω_{IF} is a function of the system properties and response and is a measure of the preferred vibration frequency of a dynamic system. The ω_{IF} of a linear primary structure remains constant over all time, regardless of the response of the structure, and is the same as the natural frequency of the structure itself. However, the ω_{IF} of a nonlinear system is not necessarily constant and can vary continuously with the response of the system.

There are numerous potential approaches that could be used to determine the ω_{IF} (Frank Pai 2010; Huang et al. 2009; Wang and Gao 2013). Although most of these approaches are based on the assumption that system data corresponds to a linear dynamic response, the ω_{IF} can be used as a tool to characterize specific dynamic systems along their nonlinear time-history response (Moaveni and Asgarieh 2012). This study uses a method in which instantaneous modal parameters are produced from an eigen analysis using the linearized system properties of the nonlinear structure (i.e., tangent stiffness matrix and tangent mass matrix). Details on the process use to determine ω_{IF} at each time instant are presented below.

In a nonlinear structure, the general force equilibrium equation can be presented by

$$\mathbf{P}_{ext} = \mathbf{F}_{int}(\mathbf{u}, \dot{\mathbf{u}}, \ddot{\mathbf{u}}) \tag{15}$$

where $\mathbf{P}_{ext}$ contains the externally applied loads and $\mathbf{F}_{int}$ contains the internal forces, which are functions of the system degrees of freedom (DOF) $(\mathbf{u}_0)$ and the derivatives of those DOF $(\dot{\mathbf{u}}_0, \ddot{\mathbf{u}}_0)$. Any nonlinear equilibrium equation can be linearized by perturbing the force about a known set of evaluation points, $\mathbf{u}_0$, $\dot{\mathbf{u}}_0$, and $\ddot{\mathbf{u}}_0$. A small perturbation in the applied load corresponds to a perturbation in the nodal DOFs, and a first-order Taylor series expansion of the internal forces is expressed as

$$\mathbf{P}_{ext} + d\mathbf{P} = \mathbf{F}_{int}(\mathbf{u}_0, \dot{\mathbf{u}}_0, \ddot{\mathbf{u}}_0) + \frac{\partial \mathbf{F}_{int}}{\partial \mathbf{u}}\Big|_{\substack{\mathbf{u}=\mathbf{u}_0,\\ \dot{\mathbf{u}}=\dot{\mathbf{u}}_0,\\ \ddot{\mathbf{u}}=\ddot{\mathbf{u}}_0}} d\mathbf{u} + \frac{\partial \mathbf{F}_{int}}{\partial \dot{\mathbf{u}}}\Big|_{\substack{\mathbf{u}=\mathbf{u}_0,\\ \dot{\mathbf{u}}=\dot{\mathbf{u}}_0,\\ \ddot{\mathbf{u}}=\ddot{\mathbf{u}}_0}} d\dot{\mathbf{u}} + \frac{\partial \mathbf{F}_{int}}{\partial \ddot{\mathbf{u}}}\Big|_{\substack{\mathbf{u}=\mathbf{u}_0,\\ \dot{\mathbf{u}}=\dot{\mathbf{u}}_0,\\ \ddot{\mathbf{u}}=\ddot{\mathbf{u}}_0}} d\ddot{\mathbf{u}} \tag{16}$$

As $\mathbf{u}_0$, $\dot{\mathbf{u}}_0$, and $\ddot{\mathbf{u}}_0$ satisfy Eq. (15), Eq. (16) can be reduced to

$$\begin{aligned} d\mathbf{P} &= \left(\frac{\partial \mathbf{F}_{int}}{\partial \mathbf{u}}\Big|_{\substack{\mathbf{u}=\mathbf{u}_0,\\ \dot{\mathbf{u}}=\dot{\mathbf{u}}_0,\\ \ddot{\mathbf{u}}=\ddot{\mathbf{u}}_0}}\right) d\mathbf{u} + \left(\frac{\partial \mathbf{F}_{int}}{\partial \dot{\mathbf{u}}}\Big|_{\substack{\mathbf{u}=\mathbf{u}_0,\\ \dot{\mathbf{u}}=\dot{\mathbf{u}}_0,\\ \ddot{\mathbf{u}}=\ddot{\mathbf{u}}_0}}\right) d\dot{\mathbf{u}} + \left(\frac{\partial \mathbf{F}_{int}}{\partial \ddot{\mathbf{u}}}\Big|_{\substack{\mathbf{u}=\mathbf{u}_0,\\ \dot{\mathbf{u}}=\dot{\mathbf{u}}_0,\\ \ddot{\mathbf{u}}=\ddot{\mathbf{u}}_0}}\right) d\ddot{\mathbf{u}} \\ d\mathbf{P} &= [\mathbf{K}_t(\mathbf{u}_0, \dot{\mathbf{u}}_0, \ddot{\mathbf{u}}_0)] d\mathbf{u} + [\mathbf{C}_t(\mathbf{u}_0, \dot{\mathbf{u}}_0, \ddot{\mathbf{u}}_0)] d\dot{\mathbf{u}} \\ &+ [\mathbf{M}_t(\mathbf{u}_0, \dot{\mathbf{u}}_0, \ddot{\mathbf{u}}_0)] d\ddot{\mathbf{u}} \end{aligned} \tag{17}$$

where $\mathbf{K}_t(\mathbf{u}, \dot{\mathbf{u}}, \ddot{\mathbf{u}})$, $\mathbf{C}_t(\mathbf{u}, \dot{\mathbf{u}}, \ddot{\mathbf{u}})$, and $\mathbf{M}_t(\mathbf{u}, \dot{\mathbf{u}}, \ddot{\mathbf{u}})$ are the tangent stiffness, tangent damping, and tangent mass matrices, respectively. These matrices can be expressed as follows for an n degree of freedom system.

$$[\mathbf{K}_t(\mathbf{u}, \dot{\mathbf{u}}, \ddot{\mathbf{u}})] = \frac{\partial \mathbf{F}_{int}}{\partial \mathbf{u}} = \begin{bmatrix} \frac{\partial \mathbf{F}_{int,1}}{\partial \mathbf{u}_1} & \frac{\partial \mathbf{F}_{int,1}}{\partial \mathbf{u}_2} & \cdots & \frac{\partial \mathbf{F}_{int,1}}{\partial \mathbf{u}_n} \\ \frac{\partial \mathbf{F}_{int,2}}{\partial \mathbf{u}_1} & \frac{\partial \mathbf{F}_{int,2}}{\partial \mathbf{u}_2} & \cdots & \frac{\partial \mathbf{F}_{int,2}}{\partial \mathbf{u}_n} \\ \vdots & \vdots & \ddots & \vdots \\ \frac{\partial \mathbf{F}_{int,n}}{\partial \mathbf{u}_1} & \frac{\partial \mathbf{F}_{int,n}}{\partial \mathbf{u}_2} & \cdots & \frac{\partial \mathbf{F}_{int,n}}{\partial \mathbf{u}_n} \end{bmatrix} \tag{18}$$

$$[\mathbf{C}_t(\mathbf{u}, \dot{\mathbf{u}}, \ddot{\mathbf{u}})] = \frac{\partial \mathbf{F}_{int}}{\partial \dot{\mathbf{u}}} = \begin{bmatrix} \frac{\partial \mathbf{F}_{int,1}}{\partial \dot{\mathbf{u}}_1} & \frac{\partial \mathbf{F}_{int,1}}{\partial \dot{\mathbf{u}}_2} & \cdots & \frac{\partial \mathbf{F}_{int,1}}{\partial \dot{\mathbf{u}}_n} \\ \frac{\partial \mathbf{F}_{int,2}}{\partial \dot{\mathbf{u}}_1} & \frac{\partial \mathbf{F}_{int,2}}{\partial \dot{\mathbf{u}}_2} & \cdots & \frac{\partial \mathbf{F}_{int,2}}{\partial \dot{\mathbf{u}}_n} \\ \vdots & \vdots & \ddots & \vdots \\ \frac{\partial \mathbf{F}_{int,n}}{\partial \dot{\mathbf{u}}_1} & \frac{\partial \mathbf{F}_{int,n}}{\partial \dot{\mathbf{u}}_2} & \cdots & \frac{\partial \mathbf{F}_{int,n}}{\partial \dot{\mathbf{u}}_n} \end{bmatrix} \tag{19}$$

$$[\mathbf{M}_t(\mathbf{u}, \dot{\mathbf{u}}, \ddot{\mathbf{u}})] = \frac{\partial \mathbf{F}_{int}}{\partial \ddot{\mathbf{u}}} = \begin{bmatrix} \frac{\partial \mathbf{F}_{int,1}}{\partial \ddot{\mathbf{u}}_1} & \frac{\partial \mathbf{F}_{int,1}}{\partial \ddot{\mathbf{u}}_2} & \cdots & \frac{\partial \mathbf{F}_{int,1}}{\partial \ddot{\mathbf{u}}_n} \\ \frac{\partial \mathbf{F}_{int,2}}{\partial \ddot{\mathbf{u}}_1} & \frac{\partial \mathbf{F}_{int,2}}{\partial \ddot{\mathbf{u}}_2} & \cdots & \frac{\partial \mathbf{F}_{int,2}}{\partial \ddot{\mathbf{u}}_n} \\ \vdots & \vdots & \ddots & \vdots \\ \frac{\partial \mathbf{F}_{int,n}}{\partial \ddot{\mathbf{u}}_1} & \frac{\partial \mathbf{F}_{int,n}}{\partial \ddot{\mathbf{u}}_2} & \cdots & \frac{\partial \mathbf{F}_{int,n}}{\partial \ddot{\mathbf{u}}_n} \end{bmatrix} \tag{20}$$

Accordingly, the tangent stiffness and tangent mass matrices of the structure with the VIRM considered in this study are defined as

$$\begin{aligned}\mathbf{M_t} &= \begin{bmatrix} \frac{\partial F_1}{\partial \ddot{u}} & \frac{\partial F_1}{\partial \ddot{x}} \\ \frac{\partial F_2}{\partial \ddot{u}} & \frac{\partial F_2}{\partial \ddot{x}} \end{bmatrix} \\ &= \begin{bmatrix} m_s + n\left(\frac{1}{12}m_{sd}\left(\frac{3}{4}{d_{sd}}^2 + {h_{sd}}^2\right) + \frac{1}{2}m_c r^2\right)\alpha^2 + nm_{sd}x^2\alpha^2 & 0 \\ 0 & m_{sd} \end{bmatrix} \\ \mathbf{K_t} &= \begin{bmatrix} \frac{\partial F_1}{\partial u} & \frac{\partial F_1}{\partial x} \\ \frac{\partial F_2}{\partial u} & \frac{\partial F_2}{\partial x} \end{bmatrix} \\ &= \begin{bmatrix} k_s & 2nm_{sd}\dot{x}\alpha^2\dot{u} + 2nm_{sd}x\alpha^2\ddot{u} \\ 0 & -m_{sd}\alpha^2\dot{u}^2 + k_{sd} \end{bmatrix}\end{aligned} \quad (21)$$

In the above equation for $\mathbf{K_t}$, k_{sd} is replaced by k_p when the penalty spring becomes engaged, i.e., if $x<R_{lbc}$ or $x\geq R_{ubc}$.

Using the above equations, linearized mass and stiffness matrices are produced at each time step in the simulation. Finally, an eigenvalue analysis is performed at each time step with $\mathbf{M_t}$ and $\mathbf{K_t}$ to estimate the ω_{IF} of the system. As the system with a VIRM is a 2DOF system, two natural frequencies will result. The ω_{IF} considered in this measure is defined as the frequency with more substantial engagement of the primary structure in its mode shape.

3.2 Weighted average instantaneous frequency

While ω_{IF} varies over time, a single measure can be derived from the time history of ω_{IF} that provides information on the overall behavior of the system. One of these measures is $\bar{\omega}_w$, the weighted average value of ω_{IF}. To calculate $\bar{\omega}_w$, the time-history of the total energy of the structure is considered as the weight. The weighted average instantaneous frequency can be calculated as

$$\varpi_w = \frac{\sum_{i=1}^{N} W_i \omega_{IF,i}}{\sum_{i=1}^{N} W_i} \quad (22)$$

where W_i and $\omega_{IF,i}$ are the total energy and ω_{IF} of the structure at time step i, respectively, and N is the total number of time steps in the response considered. When computing the weighted average instantaneous frequency, the total energy includes the energy in the structure and the energy in the VIRM or FIRM attached to the structure. As ω_{IF} is constant for the structure with the FIRM, $\bar{\omega}_w$ and ω_{IF} have the same value for the structure with the FIRM.

3.3 Overall fundamental frequency

Similar to $\bar{\omega}_w$, the overall fundamental frequency, ω_0, can be used to evaluate a system's total dynamic response by identifying the response's lowest dominant frequency component. While ω_0 would not change for a linear system, it can shift due to changes in the loading type and loading amplitude for a nonlinear system.

In this study, estimated auto power spectral densities (APSDs) of resulting numerically simulated primary structure displacement time-histories are utilized to identify ω_0 of the structure. These estimated APSDs are produced using Welch's averaged, modified periodogram method of spectral estimation (MathWorks 2022b). As the APSD of a response can vary with the duration of the response considered, the time-history signal duration chosen for each analysis was 100 seconds. For harmonic and white noise loading, a Hanning window with a number of points equal to one tenth of the dataset length is applied and a 50% overlap ratio is utilized. For the initial displacement condition, a 0% overlap ratio is utilized and an exponential window with a length of the same number of points as the dataset and an exponential decay constant of 0.5.

The highest peak at a non-zero frequency in the APSD function for the primary structure's displacement response is defined in this study as ω_0 when considering the white noise loading or an initial displacement. For a generalized harmonic loading, the highest peak of the auto-spectrum would not necessarily yield the actual ω_0 of the system as the highest peak could instead come from the frequency of the forcing function. Consequently, an alternative definition of ω_0 is used in this paper for the harmonic loading case. For harmonic loading, the ω_0 is defined as the loading frequency that results in the largest peak APSD value. This measure can be thought of as a pseudo resonance frequency and is evaluated by considering the response and resulting APSD to harmonic loading over a range of loading frequencies.

3.4 H_2 Norm Analog

The H_2 quantifies variance amplification and can be utilized to assess the impact of the VIRM on the normalized primary structure displacement amplitude under dynamic loading. When the structure is subjected to a loading *p(t)* and its response output is *z(t)*, the H_2 of the structure is defined by

$$H_2 = \sqrt{\frac{1}{2\pi}\int_{-\infty}^{\infty} \left|H_{zp}(j\omega)\right|^2 d\omega} \quad (23)$$

where $H_{zp}(j\omega)$ is the frequency domain transfer function between the loading and response.

For a linear time invariant system with an analytically determined transfer function, the H_2 can be determined using Eq. (23). However, the same approach cannot be applied to a nonlinear structure like the structure in this study as an analytical transfer function is not available. Consequently, this study considers an H_2 analog value as a response measure, which is denoted as $\tilde{H}_2$. For the initial displacement and harmonic loading case, $\tilde{H}_2$ is determined

by taking the square of the area under the estimated APSD function for the structure's displacement response between 0 rad/sec and the Nyquist frequency. For the random force excitation case, the estimated transfer function is used to produce $\tilde{H}_2$ instead of the APSD curve.

Normalized values of $\tilde{H}_2$ can then be produced. For the initial displacement and white noise cases, the $\tilde{H}_2$ of the structure with the VIRM is normalized by the $\tilde{H}_2$ of the structure with the FIRM. For the harmonic loading case, the maximum $\tilde{H}_2$ from the analyzed range of loading frequencies with the structure with the VIRM is identified and normalized by the identified maximum $\tilde{H}_2$ for the structure with the FIRM. The normalized $\tilde{H}_2$ response measure (Σ), can be expressed as

$$\Sigma = \frac{\tilde{H}_2(\text{VIRM})}{\tilde{H}_2(\text{FIRM (at } x_0))} \quad (24)$$

4 Instantaneous frequency

To investigate the dynamic effects of the VIRM on the primary structure, this section presents and explores examples of the variation in the $\Psi_{\omega_{IF}}$ of the primary structure with a VIRM subjected to various loading types, loading amplitudes, and loading frequencies and for ranges of slider mass damping. The loads considered in this section are initial conditions, harmonic loading, and white noise. As the structure with the VIRM is nonlinear in nature, the $\Psi_{\omega_{IF}}$ continuously varies over time. To provide points of comparison, the $\Psi_{\omega_{IF}}$ of the structure with the FIRM is provided when the sliders are locked at the initial position (denoted as FIRM (at x_0)) and when the sliders are locked at the R_{ubc} position (denoted as FIRM (at R_{ubc})). Note that the structure with the FIRM (at R_{ubc}) will have a lower $\Psi_{\omega_{IF}}$ than the structure with the FIRM (at x_0) as the slider masses fixed at the R_{ubc} position results in a higher moment of inertia. Fig. 3 presents the effect of different load types on the $\Psi_{\omega_{IF}}$ of VIRM and FIRM structural configurations, where, the VIRM structure has a linearized slider damping ratio of 4 (ξ_{sd}=4). Fig. 3(a) shows that for the initial displacement, the structure with the VIRM has a $\Psi_{\omega_{IF}}$ of 0.96 initially, identical to the constant $\Psi_{\omega_{IF}}$ of the structure with the FIRM (at x_0), as expected. As the structure responds to the displacement initial condition, the $\Psi_{\omega_{IF}}$ oscillates between about 0.96 and 0.84 for several cycles, then the amplitude of the changes in the $\Psi_{\omega_{IF}}$ reduce and the $\Psi_{\omega_{IF}}$ remains around 0.96.

The shifts in the $\Psi_{\omega_{IF}}$ observed in Fig. 3(a) with the VIRM are because of the movement of the slider masses within the VIRM flywheel. The effective force on the slider masses is related to the velocity of the flywheel; thus, oscillations in the response of the structure result in oscillations in the force on and radial displacement response of the slider masses. As the $\Psi_{\omega_{IF}}$ is inversely related to the moment of inertia of the structure, the $\Psi_{\omega_{IF}}$ holds an inverse analog relationship with the slider mass displacement. When the slider masses reach the furthest into the penalty spring region, the VIRM generates a higher moment of inertia than any other orientation of the slider masses and the structure with the VIRM has the lowest observed $\Psi_{\omega_{IF}}$. Note that, while the high stiffness of the penalty spring helps to restrain excessive displacements of the slider mass, the model of the system does not consider a fixed maximum allowable position of the slider masses; thus, the lowest possible $\Psi_{\omega_{IF}}$ of the structure could vary depending on the system's parameters and applied excitation. Additionally, the dynamic response of the structure to this initial displacement dissipates due to damping in the system and the $\Psi_{\omega_{IF}}$ returns to 0.96 with the slider masses coming to rest at their initial positions. Fig. 3(b-c) also show that the $\Psi_{\omega_{IF}}$ continuously shifts between 0.96 to 0.8 and 0.96 to 0.65 for the harmonic loading case and white noise case, respectively. However, as the harmonic loading and white noise on the structure continues during the entire analysis, the structure does not converge to a constant $\Psi_{\omega_{IF}}$ like the initial displacement case.

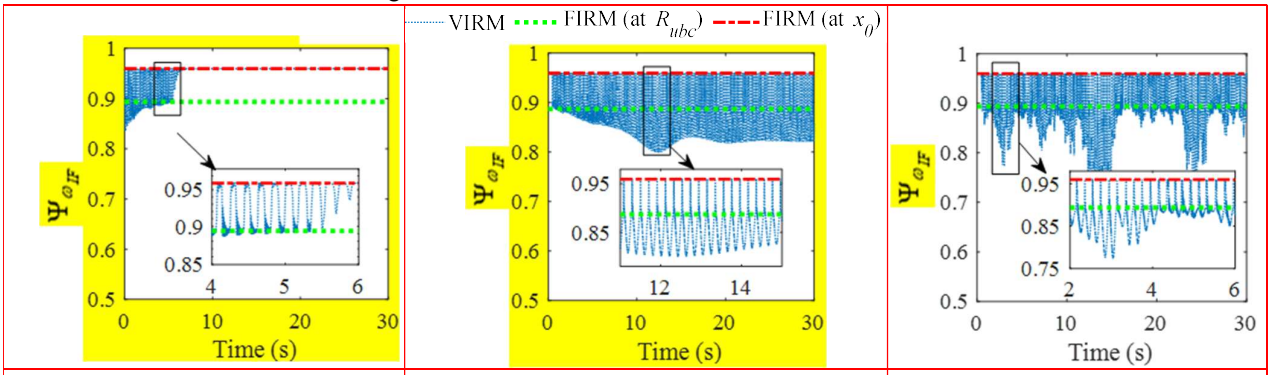

(a) Initial displacement = 1 m

(b) Harmonic loading with normalized amplitude of 0.05 m at a loading frequency ratio of 0.85

(c) White noise with normalized RMS amplitude of 0.3 m

Fig. 3 Normalized instantaneous frequency, $\Psi_{\omega_{IF}}$, of the primary structure with the VIRM (linearized slider damping ratio, ξ_{sd}=4) and the FIRMs for different loading types

In order to investigate the effect of slider damping for different types of loading, the $\Psi_{\omega_{IF}}$ time histories considering undamped (zero slider damping), low damped, and highly damped slider masses are shown in Fig. 4, Fig. 5, and Fig. 6 for the initial displacement, harmonic loading and white noise cases, respectively. The displacement response of the primary structure is also illustrated in the figures for all the damping levels. Note that all structures analyzed, even with the undamped slider masses, have the same 2% inherent damping in the primary structure. Additionally, low damping and high damping scenarios indicate a linearized slider damping ratio, ξ_{sd}, of 0.13 and 20.05, respectively in all the figures mentioned above. Due to the nonlinear nature of the VIRM, the ξ_{sd} is not the same as the damping ratio in general. Rather, the effect of a given value of ξ_{sd} will vary depending on the radial position of the slider masses and relative velocity of the primary structure. Consequently, values of ξ_{sd} greater than 1 do not necessarily mean the slider should behave in an overdamped manner.

It can be observed Fig. 4 that the $\Psi_{\omega_{IF}}$ begins to oscillate with a maximum value consistently around 0.96. In the zero slider damping case, the $\Psi_{\omega_{IF}}$ reaches a minimum value of around 0.82 quickly after the initial displacement. As the displacement response of the structure with zero slider damping decays due to inherent structural damping, the minimum value of the $\Psi_{\omega_{IF}}$ increases until about 12 seconds into the response. After this point, the displacement of the structure has mostly attenuated, but sustained oscillations between about 0.96 and 0.91 remain in the $\Psi_{\omega_{IF}}$. These sustained oscillations in $\Psi_{\omega_{IF}}$ are because energy is trapped in the undamped sliders, but cannot transfer back to the primary structure because the primary structure is no longer effectively responding dynamically. When damping is introduced to the slider mass, the fluctuations in the $\Psi_{\omega_{IF}}$ cease after some time and return to their initial values. For instance, in the low damping case, the $\Psi_{\omega_{IF}}$ changes from 0.96 to 0.82 for the first 5 s and smoothly transitions to have a constant $\Psi_{\omega_{IF}}$ of 0.96. When the slider masses are heavily damped, the sliders are restrained from moving rapidly. In this case, the $\Psi_{\omega_{IF}}$ initially keeps changing, but over a narrower frequency range before it finally progresses to a constant 0.96 as the movement of the sliders cease. In this high slider damping case, the $\Psi_{\omega_{IF}}$ of the structure with the VIRM initially oscillates between 0.84 and 0.91, then the $\Psi_{\omega_{IF}}$ shifts between 0.91 and 0.93 at around 5 s, and then steadily converges to 0.96. The displacement response of the primary structure reduces to zero around the same time for the damped cases as the undamped slider case because most of the energy of the structure is dissipated by the structure's inherent damping.

The $\Psi_{\omega_{IF}}$ and the displacement time history of the structure given different slider damping levels under harmonic loading are plotted in Fig.. For all the slider

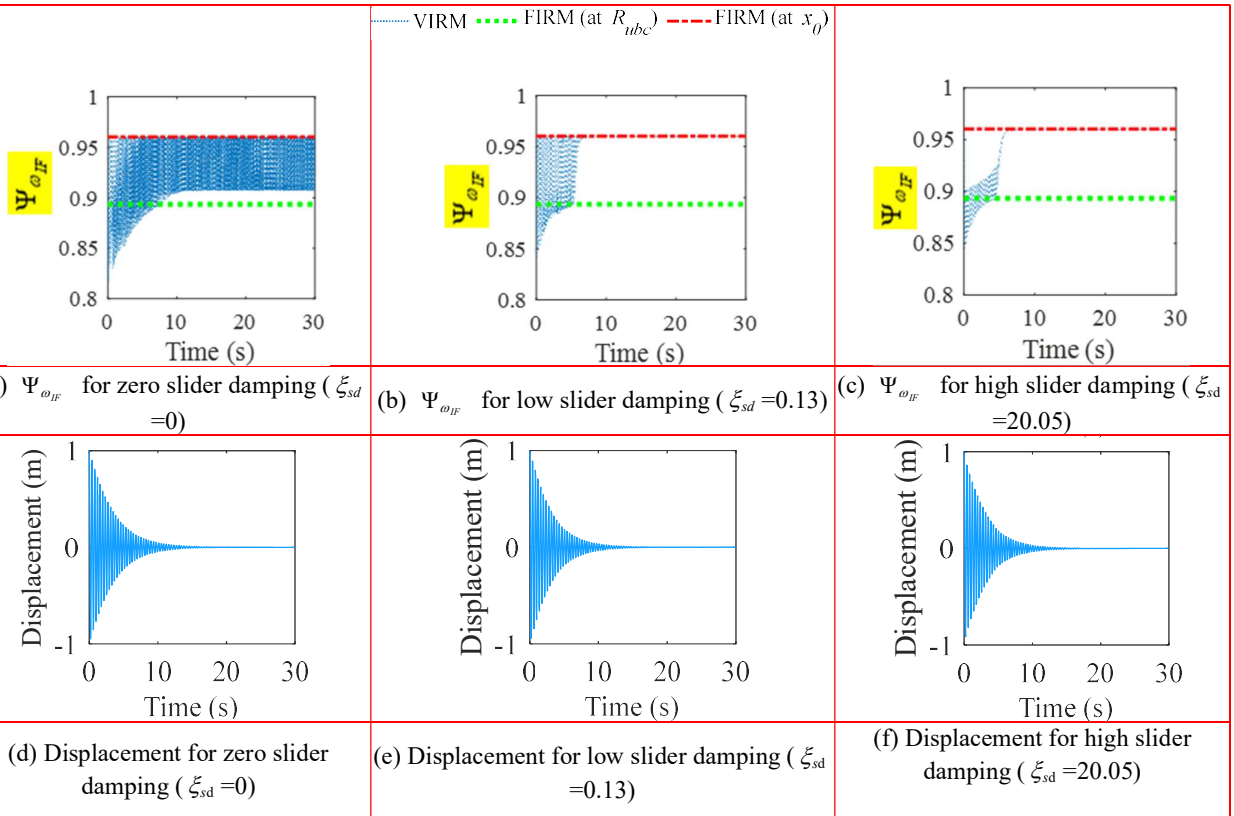

(a) $\Psi_{\omega_{IF}}$ for zero slider damping (ξ_{sd} =0)

(b) $\Psi_{\omega_{IF}}$ for low slider damping (ξ_{sd} =0.13)

(c) $\Psi_{\omega_{IF}}$ for high slider damping (ξ_{sd} =20.05)

(d) Displacement for zero slider damping (ξ_{sd} =0)

(e) Displacement for low slider damping (ξ_{sd} =0.13)

(f) Displacement for high slider damping (ξ_{sd} =20.05)

Fig. 4 Effect of slider damping on the normalized instantaneous frequency, $\Psi_{\omega_{IF}}$, and displacement of the primary structure for an initial displacement=1 m

damping levels, the loading frequency was selected such that it results in the largest total response. This figure shows that the $\Psi_{\omega_{IF}}$ oscillates and changes with time for all the slider damping levels. When the slider masses are undamped, the $\Psi_{\omega_{IF}}$ shifts between a range of 0.96 and 0.78 and includes some abrupt changes in the lower bound envelope of the $\Psi_{\omega_{IF}}$. It is also observed that the $\Psi_{\omega_{IF}}$ oscillates between 0.96 and 0.80 for the low damping level and achieves a much smoother lower bound envelope of $\Psi_{\omega_{IF}}$. Furthermore, the $\Psi_{\omega_{IF}}$ shifts between 0.91 and 0.81 in the highly damped slider mass case after a short amount of time. The overall reduction in the upper value of $\Psi_{\omega_{IF}}$ in the high damped case is because the high damping makes the slider mass less responsive; the slider is not able to quickly return each cycle to the x_0 position and the slider movement ends up restricted to the penalty spring region near the upper bound. This figure also shows that the displacement response and $\Psi_{\omega_{IF}}$ reach mostly steady state behavior after about 25 seconds in both the slider damping cases.

Fig. 6 shows the $\Psi_{\omega_{IF}}$ and the time-history of the displacement of the structure for different slider damping levels with a white noise loading with a normalized RMS amplitude of 0.3 m. This figure shows that the $\Psi_{\omega_{IF}}$ shifts between 0.96 and 0.65 for the zero slider damping case and the lower bound envelope of the $\Psi_{\omega_{IF}}$ rapidly changes. With the small amount of slider damping that is added to the VIRM in the low slider damping case, the $\Psi_{\omega_{IF}}$ looks much the same, but with a slight increase in the overall lower value of the $\Psi_{\omega_{IF}}$. Even in the high slider damping case, the lower envelope of the $\Psi_{\omega_{IF}}$ changes rapidly due to the continuous but random loading. However, for the high slider damping case, the $\Psi_{\omega_{IF}}$ primarily oscillates between 0.91 and 0.7 and it does not reach the initial $\Psi_{\omega_{IF}}$ value of 0.96 again similar to the harmonic loading case as presented Fig. 6(c). Fig. 6 also shows that the $\Psi_{\omega_{IF}}$ is related to the response amplitude of the primary structure. For example, in all cases, the lowest $\Psi_{\omega_{IF}}$ occurs around 13 seconds, when the primary structure experiences its maximum response.

The influence of the slider damping on the dissipation of energy is illustrated in Fig. 7. This figure presents the energy dissipated by the slider damping, as a percentage of the total energy dissipated, versus ξ_{sd} for different loading types. For this analysis, a unit displacement, a harmonic loading with a normalized amplitude of 0.05 m at the pseudo resonance frequency, and a white noise of normalized RMS amplitude of 0.3 m are applied to the structure separately. For the initial displacement loading, this figure shows that as the

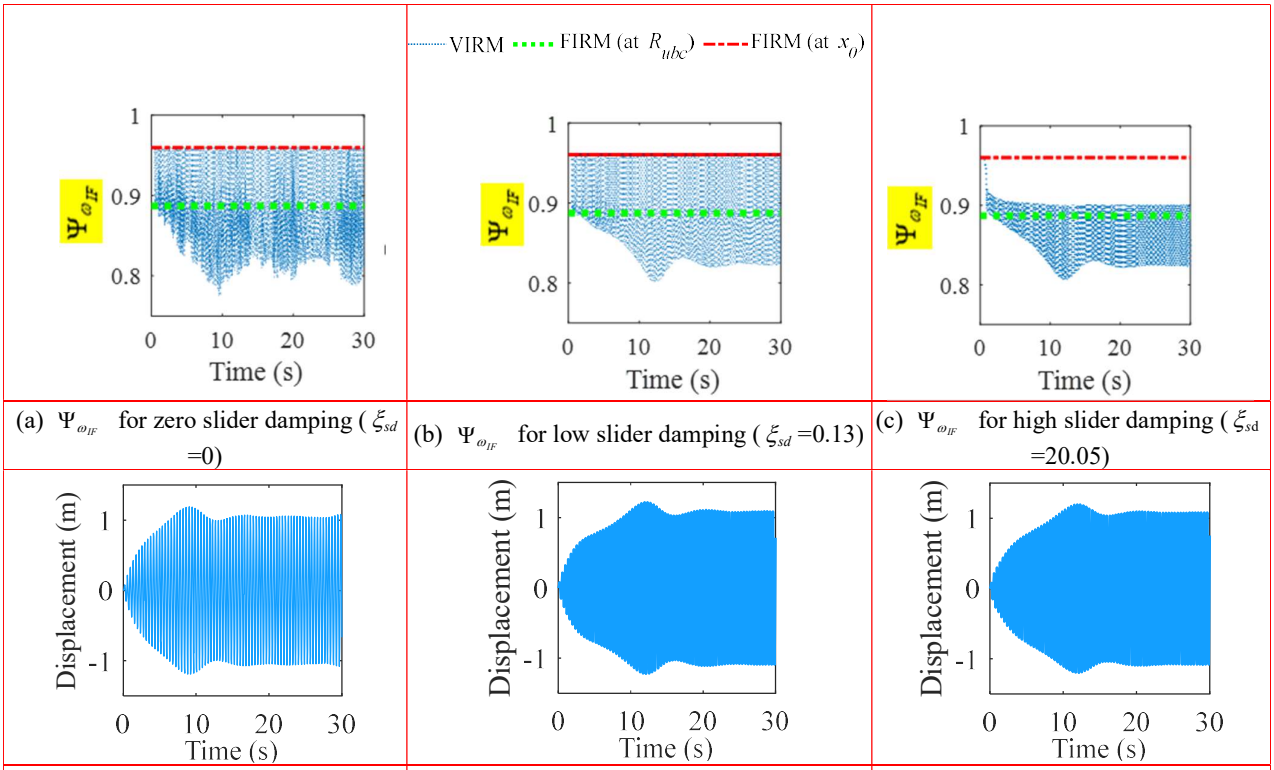

(a) $\Psi_{\omega_{IF}}$ for zero slider damping (ξ_{sd} =0)

(b) $\Psi_{\omega_{IF}}$ for low slider damping (ξ_{sd} =0.13)

(c) $\Psi_{\omega_{IF}}$ for high slider damping (ξ_{sd} =20.05)

(d) Displacement for zero slider damping (ξ_{sd} =0)

(e) Displacement for low slider damping (ξ_{sd} =0.13)

(f) Displacement for high slider damping (ξ_{sd} =20.05)

Fig. 5 Effect of slider damping on the normalized instantaneous frequency, $\Psi_{\omega_{IF}}$, and displacement of the primary structure for harmonic loading with normalized amplitude of 0.05 m at load frequency ratio of 0.86 (zero slider damping) or 0.85 for both slider damping cases

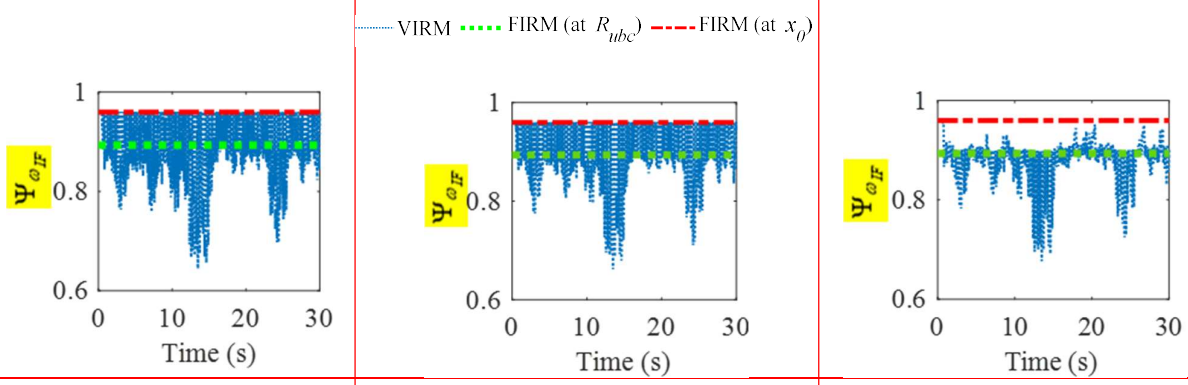

(a) $\Psi_{\omega_{IF}}$ for zero slider damping (ξ_{sd} =0)

(b) $\Psi_{\omega_{IF}}$ for low slider damping (ξ_{sd} =0.13)

(c) $\Psi_{\omega_{IF}}$ for high slider damping (ξ_{sd} =20.05)

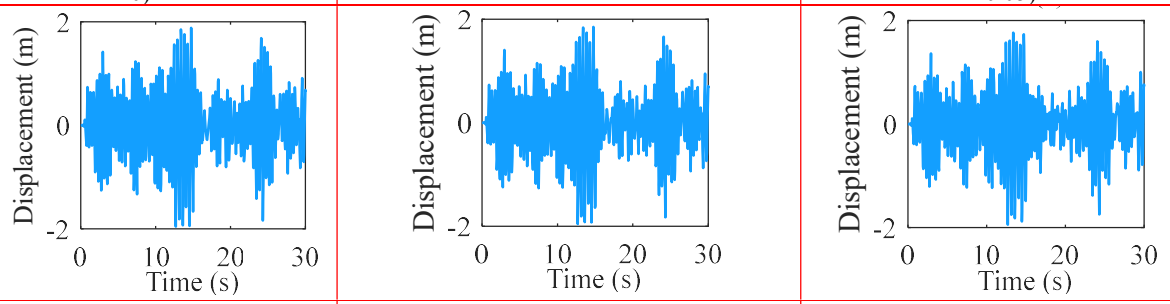

(d) Displacement for zero slider damping (ξ_{sd} =0),

(e) Displacement for low slider damping (ξ_{sd} =0.13)

(f) Displacement for high slider damping (ξ_{sd} =20.05)

Fig. 6 Effect of slider damping on the normalized instantaneous frequency, $\Psi_{\omega_{IF}}$, and displacement of the primary structure for white noise with normalized RMS amplitude of 0.3 m

slider damping increases, the dissipated energy percentage increases and reaches a maximum of 16% when ξ_{sd} is 1.34. Afterwards the dissipation percentage slightly decreases to 14% and stays similar for higher slider damping. A similar trend is also noticed for the harmonic loading case with a maximum energy dissipation of 11% for ξ_{sd} of 0.67 and a close to 5% dissipation for higher slider damping. For the white noise case, there is an initial peak of 10.27% in dissipated energy percentage at ξ_{sd} of 0.80. This is followed by a rapid reduction in dissipation percentage until ξ_{sd} is 1.34, then a long increase in dissipation percentage when ξ_{sd} is higher than 1.34. For example, when ξ_{sd} increases from 6.68 to 13.36, the dissipation percentage increases from 10.78% to 19.78%.

This section explored the dynamic effects of the VIRM on the primary structure's instantaneous frequency, $\Psi_{\omega_{IF}}$, under various loading conditions, and slider damping levels. The changes in VIRM $\Psi_{\omega_{IF}}$ were compared with the frequencies of the FIRM with different flywheel configurations. The results showed the $\Psi_{\omega_{IF}}$ of the primary structure with VIRM's oscillated during the response of the structure due to slider mass movement within the flywheel. Higher slider damping generally resulted in a narrower frequency range for the oscillations in $\Psi_{\omega_{IF}}$. However, the impact of slider damping on the primary structure's displacement response was less pronounced suggesting that while slider damping influences $\Psi_{\omega_{IF}}$, it does not always translate to significant changes in overall structural response.

While only initial displacement, a specific frequency of harmonic loading, and white noise loading where considered, the results of this section give general insight on how the $\Psi_{\omega_{IF}}$ of systems would vary in other types of loadings. Other types of transient loads would result in variations in $\Psi_{\omega_{IF}}$ that attenuate. Given a periodic loading, repeated patterns in $\Psi_{\omega_{IF}}$ are expected. Sustained loads that do not have a well-defined periodicity may result in large changes in $\Psi_{\omega_{IF}}$, including durations when the variation in $\Psi_{\omega_{IF}}$ is small and durations when it is large. A key point to note, however, is that the variation in $\Psi_{\omega_{IF}}$, and thus the resulting overall system dynamics, will depend on the amplitude of the loading applied to the system. This amplitude dependent behavior will be explored in the next section.

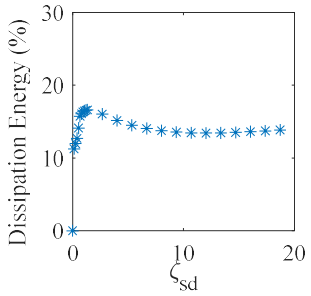

(a) Initial displacement = 1 m

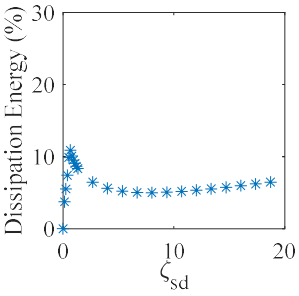

(b) Harmonic loading with normalized amplitude of 0.05 m at pseudo resonance frequency

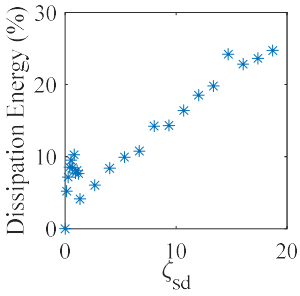

(c) White noise of RMS normalized amplitude 0.3 m

Fig. 7 Percentage of energy dissipation caused by the slider damping (linearized slider damping ratio, ξ_{sd}) for different loading types

5 Overall fundamental frequency

In this section, the effect of the VIRM on the Ψ_{ω_0} of the structure is examined. For this study, the Ψ_{ω_0} of the structure is determined based on the APSD of the displacement response of the structure, as described in Section 3.3. The Ψ_{ω_0} can be qualitatively described as the frequency the structure naturally prefers to vibrate at, which can vary due to the type and amplitude of loading for nonlinear systems. The Ψ_{ω_0} is analyzed for different loading types, loading amplitudes, loading frequencies, and for ranges of linearized slider mass damping ratios. The Ψ_{ϖ_w} is also presented in this section to compare with Ψ_{ω_0}. Moreover, the constant Ψ_{ω_0} and Ψ_{ϖ_w} of the structure with FIRM for both locked positions are provided to contrast with values of the structure with the VIRM.

Fig. 8 presents the displacement response APSDs of the primary structure for a linearized slider damping ratio of 4 with an initial displacement condition, harmonic loading, and white noise excitation. For each of the loadings in the figure, APSDs, Ψ_{ω_0} and Ψ_{ϖ_w} of the structure with the VIRM and the FIRM (at R_{ubc} and at x_0) are shown. The frequency ratio corresponding to the highest peak of the auto-spectrum, Ψ_{ω_0}, indicates the pseudo resonance frequency ratio for the structure with the VIRM. Note that Ψ_{ω_0} is the resonance frequency ratio of the structures with the FIRM. This figure shows that for an initial displacement of 1 m, the structure with the VIRM has a similar, but marginally lower peak APSD displacement amplitude compared to both structures with the FIRM (at R_{ubc} and at x_0). It is also observed that the Ψ_{ω_0} and Ψ_{ϖ_w} are lower for the structure with the VIRM than structure with the FIRMs. Additionally, Ψ_{ϖ_w} is consistent with the Ψ_{ω_0} for the structures with the FIRM, as would be expected. However, there are noticeable differences between Ψ_{ω_0} and Ψ_{ϖ_w} for the structure with the VIRM, especially for the harmonic loading (Fig. 8(b)) and white noise case (Fig. 8(c)). In the harmonic loading case, Fig. 8(b), the structures are loaded at the forcing frequencies that produced the highest peak APSD. For example, the structure with the VIRM, the FIRM (at R_{ubc}), and the FIRM (at x_0) are oscillated at load frequency ratios 0.85, 0.88 and 0.96, respectively. It is observed that the APSD of the VIRM is noisier than the FIRMs and a super harmonic pseudo resonance frequency can be noticed in the harmonic loading case. This super harmonic pseudo resonance is observed for the structure with the VIRM at a frequency ratio around 2.62 for all loading cases, but it is much more noticeable for the harmonic loading case.

Some of the trends seen in the initial displacement and harmonic loading cases are seen in the results from white noise loading in Fig. 8c. One major difference in the results for the white noise case is that in the VIRM APSD curve the Ψ_{ω_0} and the Ψ_{ϖ_w} are positioned further to the left than for the other load cases and the peak is reduced more relative to the FIRM. Another major difference in these results is that the VIRM APSD curve is more spread out. This increased spread is likely due to the broadband nature of the loading in the white noise case as well as the larger range of $\Psi_{\omega_{IF}}$ covered by the VIRM in this case. Due to this increased spread, there is expected to be more variability in the resulting identified Ψ_{ω_0} in the white noise loading case.

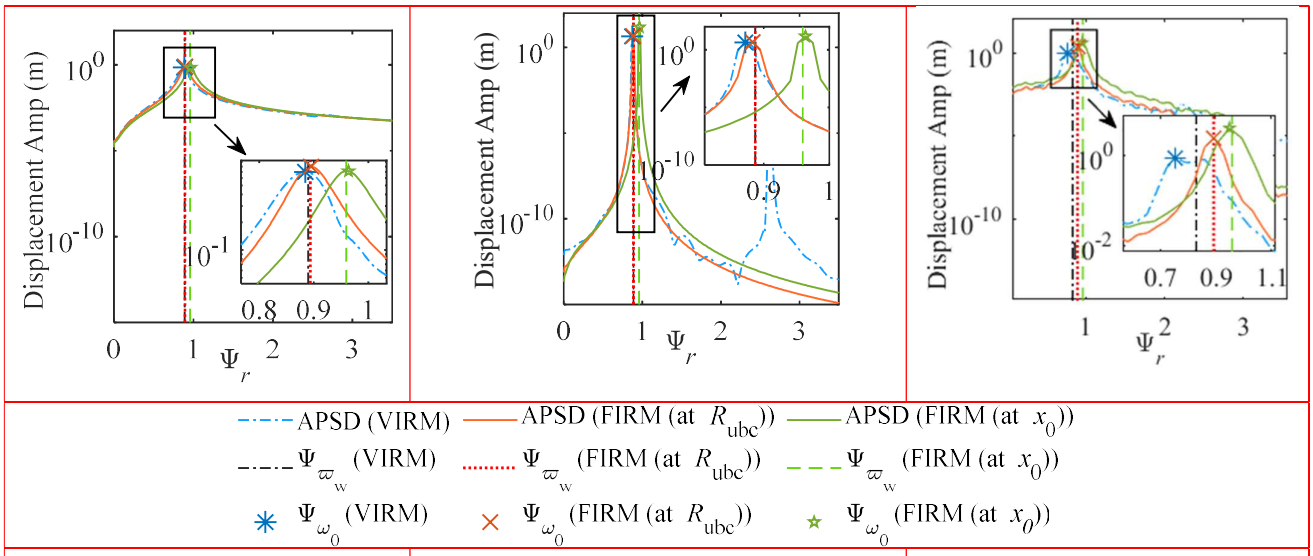

(a) Initial displacement = 1 m

(b) Normalized harmonic loading of 0.05 m at pseudo resonance/resonance frequency for the structures with the VIRM/FIRM

(c) White noise of normalized RMS amplitude of 0.3 m

Fig. 8 Auto spectral density plot and normalized weighted average instantaneous frequency, Ψ_{ϖ_w}, of the primary structure with the VIRM or the FIRM. Note that the value of normalized overall fundamental frequency, Ψ_{ω_0}, for each case is defined as the frequency ratio corresponding to that case's peak point on the auto spectral density plot.

Fig. 9 can be utilized to contrast Ψ_{ω_0} and Ψ_{ϖ_w} of the structure with the VIRM for different loading types over a range of loading amplitudes. Recall that for the harmonic loading case, Ψ_{ω_0} and Ψ_{ϖ_w} are determined using the forcing frequency that yields the maximum displacement amplitude in the frequency domain. To provide points of comparison, Ψ_{ϖ_w} for the structures with the FIRMs are also presented. As expected, Ψ_{ϖ_w} remains constant in the structures with the FIRM for each loading type as the loading amplitude does not affect the natural frequency of linear structures. However, the added mass effect from the VIRM continuously changes and depends on the loading magnitude and thus the response magnitude. Therefore, Ψ_{ω_0} and Ψ_{ϖ_w} for the VIRM vary for different loading magnitudes. It is observed that Ψ_{ω_0} and Ψ_{ϖ_w} decrease when the loading amplitude increases in nearly all cases. The decreased natural frequency for the higher amplitude load is because the resulting further extension outward of the slider masses of the VIRM adds a higher mass effect to the overall structure, which reduces the fundamental natural frequency of the structure. Although there is a similar trend between the frequency ratio and the loading amplitudes with white noise, Ψ_{ω_0} is more irregular compared to Ψ_{ϖ_w}. This is a result of the broadening of the APSD curves with white noise loading, as seen in Fig. 9. When the structure is subjected to a comparatively lower loading amplitude, Ψ_{ω_0} and Ψ_{ϖ_w} remained largely unchanged around 0.96, similar to the structure with the FIRM, where the slider masses are fixed at the initial position. In the lower loading amplitude, the slider masses do not significantly move due to the lower rotational velocity of the VIRM. At an initial displacement higher than 1.0 m and 0.9 m, Ψ_{ω_0} and Ψ_{ϖ_w} are below 0.89, respectively, which is the resonance frequency of the structure with the FIRM (at R_{ubc}). The reason that Ψ_{ω_0} and Ψ_{ϖ_w} can be lower than the resonance frequency of the structure with the FIRM (at R_{ubc}) is because the slider masses can move into the penalty spring region, causing lower $\Psi_{\omega_{IF}}$. Similarly, Ψ_{ω_0} is lower than 0.89 when the normalized harmonic loading amplitude is higher than 0.025 m and when the normalized RMS white noise amplitude is higher than 0.08 m.

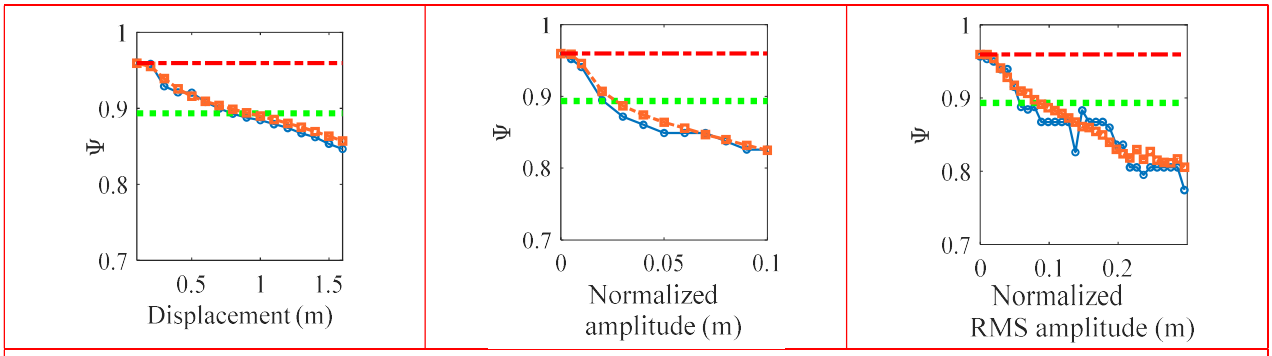

(a) Initial displacement = 1 m	(b) Structures with VIRM/FIRM excited at pseudo resonance/resonance frequency	(c) White noise excitation

Fig. 9 Normalized overall fundamental frequency, Ψ_{ω_0}, and normalized weighted average instantaneous frequency, Ψ_{ϖ_w}, of the primary structure with the VIRM (ξ_{sd} =4) and the FIRMs for different loading types and amplitudes

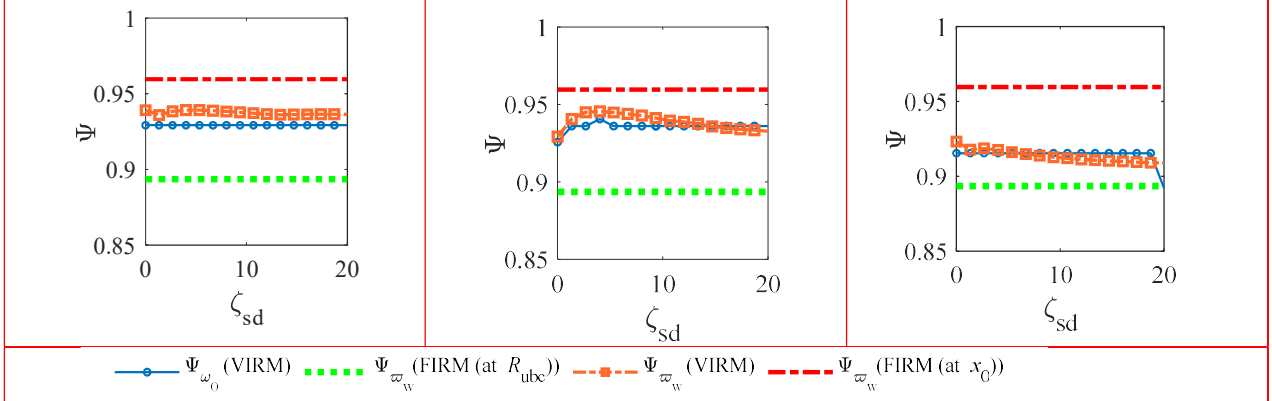

(a) Initial displacement = 0.3 m	(b) Structure with VIRM/FIRM excited at a normalized amplitude of 0.01 m at pseudo resonance/ resonance frequency	(c) White noise of normalized RMS amplitude of 0.05 m

Fig. 10 Normalized overall fundamental frequency, Ψ_{ω_0}, and normalized weighted average instantaneous frequency, Ψ_{ϖ_w}, of the primary structure with the VIRM and the FIRMs versus linearized slider damping ratio, ξ_{sd}, for different loading types

Fig. 10 presents the influence of linearized slider mass damping ratio ξ_{sd} on the Ψ_{ω_0} and Ψ_{ϖ_w} of the primary structure under an initial displacement of 0.3 m, a harmonic loading with a normalized amplitude of 0.01 m at pseudo resonance frequencies, and white noise excitation with a normalized RMS amplitude of 0.05 m. In addition, Ψ_{ϖ_w} of the structures with the FIRM are presented for comparison. It can be observed that there is an overall decreasing trend in the Ψ_{ϖ_w} for the VIRM with increasing values of ξ_{sd} for all loading types. All deviations from this trend appear minor except that in the harmonic loading case, Ψ_{ϖ_w} initially increases with increasing ξ_{sd} before it later reduces with increased ξ_{sd}. In contrast, Ψ_{ω_0} of the structure with the VIRM remains almost the same for nearly all ξ_{sd} values for each of the loading types considered. While Ψ_{ω_0} and Ψ_{ϖ_w} are very similar in nearly all cases, Ψ_{ϖ_w} is larger than Ψ_{ω_0} in all cases considered for the initial displacement loading. For the harmonic and white noise loading cases, Ψ_{ω_0} becomes larger than Ψ_{ϖ_w} as ξ_{sd} increases. While $\Psi_{\omega_{IF}}$ for the VIRM clearly varies with the slider damping level, as seen in Fig. 4, Fig. 5, and Fig. 6, the results in Fig. 9 and Fig.10 show that Ψ_{ω_0} and Ψ_{ϖ_w} are less influenced by the slider damping and more influenced by the loading amplitude changes.

This section investigates the influence of the VIRM on the primary structure's overall fundamental frequency, Ψ_{ω_0} and weighted average instantaneous frequency, Ψ_{ϖ_w} under various loading types, loading amplitudes, and slider damping levels. The analysis utilized the estimated transfer function and the auto-spectrum of the structure's displacement response to determine the Ψ_{ω_0} and the time history of $\Psi_{\omega_{IF}}$ values were used to calculate Ψ_{ϖ_w}. Comparisons of the VIRM's frequency measures are made to the frequencies of the FIRM configurations. The influence of

slider damping on Ψ_{ω_0} and Ψ_{ϖ_w} observed in this section were much less pronounced than the influence of slider damping on $\Psi_{\omega_{IF}}$ observed in the last section. Instead, loading amplitude emerged as the primary driver of changes in the VIRM's Ψ_{ω_0} and Ψ_{ϖ_w}. The results showed that the VIRM structure's Ψ_{ω_0} and Ψ_{ϖ_w} decreased as the load amplitude increased. This is due to the VIRM's variable mass effect, where larger amplitudes cause greater slider mass extension, effectively lowering the structure's effective natural frequency. These findings highlight the unique dynamic characteristics of the structure with a VIRM, where its frequency response is inherently coupled to both the amplitude and type of loading applied. Although changes in slider mass and slider stiffness are not investigated in this study, it is anticipated that through design, sets of these parameters could be chosen such that a desired shift in system natural frequency, as measured by Ψ_{ω_0} and Ψ_{ϖ_w}, could be achieved for a given load type and amplitude.

6 $\tilde{H}_2$ response measure

In this section, $\tilde{H}_2$ and Σ, which are defined in Section 3.4, are used as measures of the performance of the VIRM related to controlling the response of the primary structure. These measures will be evaluated given different types and amplitudes of loading. Furthermore, variations in these performance measures with changes in ξ_{sd} are considered in this section. As an example of how to interpret a numerical value of the normalized response measure reported in this section, a Σ of 0.6 for a VIRM configuration would indicate a 40% decrease in $\tilde{H}_2$ response measure for the structure with the VIRM relative to the structure with the FIRM at initial position, x_0.

The effect of slider mass damping on the response of the primary structure is presented in Fig. 11 and Fig. 12. Fig. 11 compares the $\tilde{H}_2$ response measure of the structure with the VIRM and the FIRMs for different ξ_{sd} values given harmonic loading with a normalized amplitude of 0.05 m. For each point along a given curve in this figure, the value of that point is the $\tilde{H}_2$ when the harmonic load has a Ψ_l equal to the x-axis value. Fig. 11 shows that for all ξ_{sd} values considered, the maximum $\tilde{H}_2$ of the structure with the VIRM occurs at a lower Ψ_l value compared to the structure with the FIRMs. This is logical as the $\tilde{H}_2$ of the structure should be greatest when it is excited at the resonance frequency for the structures with the FIRM; however, for the structure with the VIRM, the $\tilde{H}_2$ should be greatest when it is excited at the pseudo-resonance frequency and the additional added mass effects of the VIRM can shift this pseudo-resonance frequency lower than the resonance frequency of the structures with the FIRM. In addition to shifting the location of the peak value, the VIRM reduces the peak $\tilde{H}_2$ for all damping levels and also bends the $\tilde{H}_2$ curve to the lower frequency in a manner usually associated with softening systems (Nayfeh and Mook 2008).

This figure also shows that the peak values of the $\tilde{H}_2$ for the VIRM, and the Ψ_l value that results in this peak value, are all almost the same for the range of ξ_{sd} values considered.

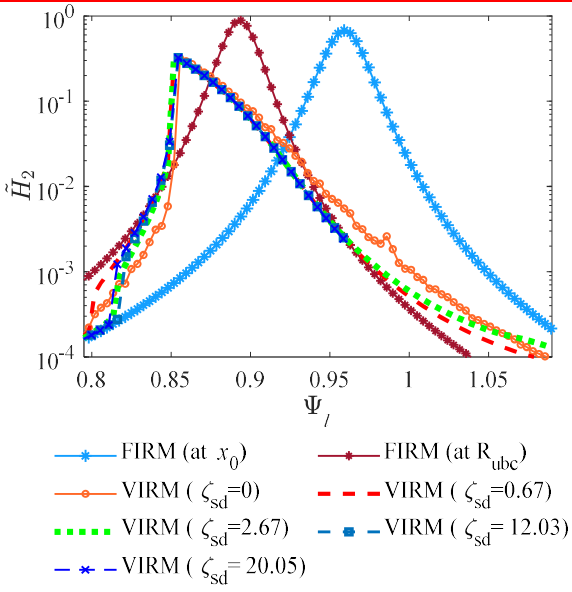

Fig. 11 $\tilde{H}_2$ of the primary structure versus loading frequency ratio, Ψ_l, with various linearized slider damping ratios, ξ_{sd}, values given a normalized harmonic loading amplitude of 0.05 m

Fig. 13 presents the normalized $\tilde{H}_2$ response measure (Σ) for the primary structure for different slider damping levels when the structure is subjected to initial displacement conditions, harmonic loading, and white noise. Note that for harmonic loading, each data point on this figure considers a range of Ψ_l values and the Σ of the structure is calculated with the maximum $\tilde{H}_2$ values for the VIRM and the FIRMs. The performance of the structures with the FIRM remains unchanged as the slider masses are locked in position. This figure shows that the structure with the VIRM consistently outperform the FIRMs under initial displacement loading for all the slider mass damping levels considered. Given the initial displacement, Σ drops when a small amount of slider damping is introduced to the VIRM. For instance, Σ decreases to 0.7 at a ξ_{sd} value of 1.34 and further decreases to 0.63 until ξ_{sd} reaches a value of 5.34. Thereafter, Σ increases once again as ξ_{sd} further increases. Similarly, the Σ is always lower than 1 for the harmonic loading and white noise case. However, in these cases Σ is much lower; for example, 0.45 and 0.63 for the harmonic and the white noise cases, respectively, when the VIRM is undamped. As ξ_{sd} increases in the harmonic loading case, Σ decreases to 0.43 when the ξ_{sd} is 1.34 and gradually increases to 0.46 at ξ_{sd} =5.34 and remains mostly unchanged in the higher slider damping range. Fig. 13(c) shows that, for the white noise case, Σ decreases as

ξ_{sd} keeps increasing. This decrease in Σ could be attributed to the continued ability of increased slider damping to dissipate more energy in this load case, as observed in Fig. 7(c).

In order to investigate the effect of loading amplitude on the performance of the structure, $\tilde{H}_2$ are plotted in Fig. 12 for harmonic loading with different amplitudes across a range of Ψ_l. This figure shows that the maximum $\tilde{H}_2$ occurs at a lower Ψ_l value for the structure with the VIRM compared to the structure with the FIRM at x_0 for the same loading amplitude, which aligns with the previous results in Fig. 11. Additionally, the structure with the FIRM at R_{ubc} location has a lower Ψ_l compared to the structure at x_0 location and has the maximum $\tilde{H}_2$ value among the three structures. At lower loading amplitudes, for example, for 0.005 m, 0.009 m and 0.02m normalized loading amplitude, the Ψ_l with the maximum $\tilde{H}_2$ is higher than the structure with the FIRM at R_{ubc}. The Ψ_l value with the maximum $\tilde{H}_2$ value of the VIRM is referred to as the pseudo resonance frequency ratio. Near the pseudo resonance frequency ratio, there are multiple stable and unstable steady-state solutions. As the structure approaches the pseudo resonance frequency ratio, the steady-state solution becomes unstable and the structure jumps to a higher stability solution. The jump amplitude of the structure depends on the load amplitude. Additionally, when the loading amplitude increases, the pseudo resonance frequency of the structure with the VIRM decreases.

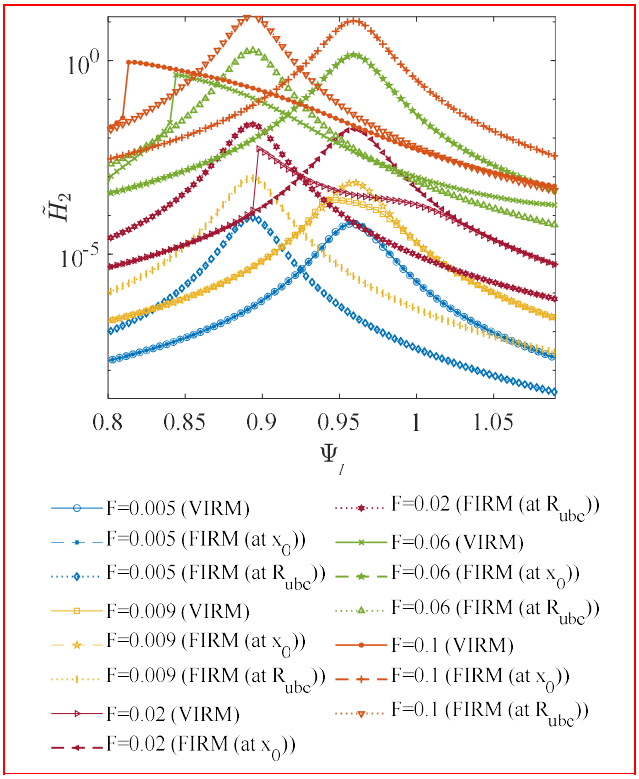

Fig. 12 $\tilde{H}_2$ of the primary structure with the VIRM (ξ_{sd} =4), the FIRM (at x_0) and the FIRM (at R_{ubc}) versus loading frequency ratio, Ψ_l, for a range of normalized harmonic loads with different normalized amplitudes, expressed in 'm'

Fig. 13 can be utilized to investigate the performance of the VIRM at different initial displacements, harmonic loading amplitudes, and white noise levels. In almost every case examined, normalized $\tilde{H}_2$ response measure is less than 1, which indicates that the VIRM is outperforming both the FIRMs. This figure shows that with a small amount of initial displacement, Σ decreases and reaches a minimum of 0.7 when the initial displacement is 0.3 m. However, Σ increases as the structure is excited with a higher initial

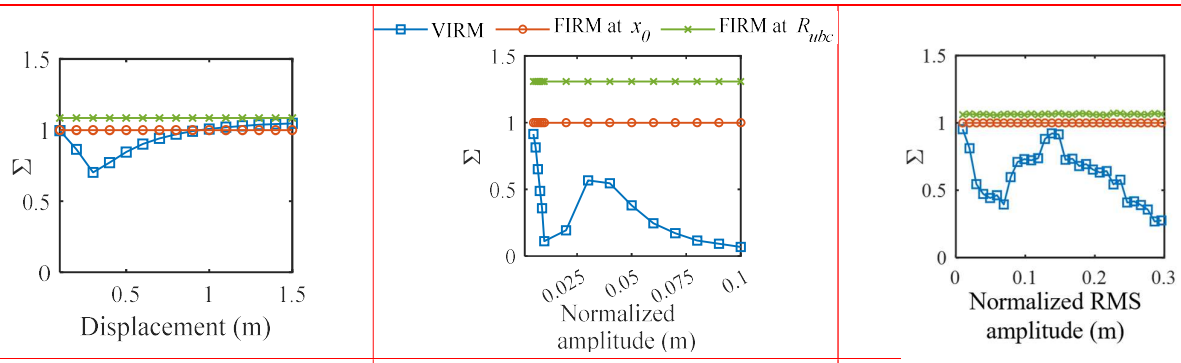

(a) Initial displacement (b) Harmonic loading (c) White noise

Fig. 13 Normalized $\tilde{H}_2$ response measure, Σ, of the structure with the VIRM (ξ_{sd} =4), the FIRM (at x_0) and the FIRM (at R_{ubc}) versus loading amplitude for different loading types

displacement beyond 0.3 m. The behavior of Σ under different loading amplitudes is very different in the harmonic loading and white noise cases compared to the initial displacement case. Σ for harmonic loading is very low (close to 0.1) for small loading amplitudes and increases with increases in the normalized loading amplitude until a peak value of Σ = 0.57 is reached, then Σ once again decreases with increased amplitude. For the white noise case, Σ decreases initially to below 0.4 when the normalized RMS amplitude is 0.07 m and increases afterwards until a normalized RMS amplitude of 0.14 m. Finally, Σ decreases again for higher normalized RMS loading beyond 0.14 m.

This section presents an evaluation of the effectiveness of the VIRM at reducing the response of the structure it is attached to using the normalized $\tilde{H}_2$ response measure, Σ, across various loading types, loading amplitudes, and slider damping levels. Comparisons of the VIRM's effectiveness are made to the effectiveness of a pair of FIRM configurations. The results in this section demonstrate that the VIRM consistently achieves lower Σ compared to the FIRMs across different load types, highlighting its effectiveness in attenuating response. While varying slider damping was found to have negligible impact on Σ, the VIRM's performance exhibit a dependence on loading amplitude, which showcases the system's inherent nonlinearity. This energy dependency will be a crucial consideration when designing VIRMs for specific applications.

While the impact of other device parameters, such as the slider mass and slider stiffness, were not investigated, it is anticipated these parameters would have a noticeable effect on the structural response as well. This impact is anticipated as these parameters would influence the effective force on the slider masses and their resistance to motion; thus, these parameters will influence the slider dynamic motion and how this motion changes with loading amplitude. These device parameters will have to be carefully considered as well when designing a VIRM.

Notably, the VIRM's effectiveness is particularly pronounced under harmonic loading, where the $\tilde{H}_2$ response measure is reduced by 90% at certain loading amplitudes compared to the FIRM at x_0. However, the VIRM's effectiveness was observed to be limited under the initial displacement loading condition, likely due to the VIRM's frequency shifting ability not being relevant in reducing the transfer of the energy into the system when a set input energy is provided in the initial displacement case. This result suggests that regardless of the parameter set chosen, it is unlikely that the VIRM will be a particularly effective choice for mitigating response to impulsive loads or initial conditions.

7 Conclusions

In this paper, an innovative passive nonlinear rotational inertial mechanism called the variable inertia rotational mechanism (VIRM) is described, formulated, and investigated. This paper examines the impact of the VIRM on the natural frequency and the response of a single-degree-of-freedom (SDOF) structure under various types of loads using numerical simulations. The following significant results were observed from this study.

- The incorporation of the VIRM in the primary structure significantly influenced the normalized instantaneous frequency ratio. Although the level of slider damping shifted the normalized instantaneous frequency ratio, the shift does not always correspond to major changes in the primary structure response. Moreover, the normalized instantaneous frequency ratio is highly dependent on the loading type and loading amplitude.
- The normalized weighted average instantaneous frequency ratio and the normalized overall fundamental frequency ratio of the structure with the VIRM reduced significantly when higher loading amplitude is applied to the structure. However, they are less influenced by the slider damping changes.
- The VIRM can notably reduce the pseudo resonance frequency ratio of the structure, and superharmonic pseudo resonances can be observed with the VIRM. Additionally, as the loading amplitude increases, the pseudo resonance frequency ratio and the $\tilde{H}_2$ response measure decrease for the structure with the

VIRM relative to the structure with the fixed inertia rotational mechanism (FIRM) at x_0 in all cases considered. The slider mass damping of the VIRM had little to no effect on the shift in the pseudo resonance frequency ratio.

- The performance of the structure with the VIRM, in terms of $\tilde{H}_2$ response measure compared to the FIRMs, changes with the slider damping level considered, but these changes are relatively small.
- The performance of the VIRM is highly dependent on the type and amplitude of the loading; however, the VIRM outperformed the FIRMs in terms of $\tilde{H}_2$ response measure in almost all the cases considered.

Overall, this paper shows that the VIRM can passively induce significant changes in the dynamics of a primary structure, as evaluated by measures related to the fundamental frequency shifts of the system. The VIRM's unique characteristics make it well-suited for employing as a structural control strategy, particularly in applications involving harmonic excitation and white noise excitation. The VIRM's performance in these load scenarios is superior compared to a FIRM due to its capacity to continuously shift the structure's effective natural frequency. This adaptive frequency not only leads to superior vibration mitigation but also helps to protect structures by preventing sustained resonance conditions. While the VIRM's dynamic frequency shifts prevent sustained resonance, it is important to acknowledge that certain loading scenarios may introduce brief periods of intensified interaction between the structure and the excitation due to the altered system frequency. Despite these interactions, the amplitude of the structural response remains bounded as resonant conditions are not maintained. The VIRM's ability to adapt a system's frequency and their two-terminal nature makes them potentially suitable for integration into structural systems in a variety of ways, including in base isolation systems, as an interstory device or in an outrigger system. However, the VIRM is likely not suitable for mitigating system responses in scenarios similar to initial displacement conditions where energy is rapidly applied to a system and the VIRM's frequency shifts cannot disrupt the flow of energy to the structure from the excitation.

Although this work with VIRM in a simplified linear model serves as a foundation for future investigation, the nonlinearity introduced by this mechanism significantly impacted the dynamics of the system. Additionally, in most circumstances investigated and with enough input amplitude, the inclusion of the VIRM results in a beneficial reduction in the system response amplitude. Thus, further research on the use of VIRM for passive control of structures, including the presence of intrinsic nonlinearities, under a variety of excitations, including seismic ground motions, is warranted. Furthermore, given the nonlinear nature of the VIRM, future studies should explore whether the system exhibits chaotic behavior, as this could offer additional insights into its effectiveness in structural control.

Acknowledgements

This research is based upon work supported by the National Science Foundation under Grant No. 1944513. Any opinions, findings, and conclusions or recommendations expressed in this material are those of the authors and do not necessarily reflect the views of the National Science Foundation.

References

Ali Sadeghian, M., J. Yang, X. Wang, and F. Wang. 2021. "Novel adaptive tuned viscous inertance damper (ATVID) with adjustable inertance and damping for structural vibration control." *Structures*, 29: 814–822. https://doi.org/10.1016/j.istruc.2020.11.050.

Brzeski, P., M. Lazarek, and P. Perlikowski. 2017. "Experimental study of the novel tuned mass damper with inerter which enables changes of inertance." *Journal of Sound and Vibration*, 404: 47–57. https://doi.org/10.1016/j.jsv.2017.05.034.

Chen, M. Z. Q., Y. Hu, L. Huang, and G. Chen. 2014. "Influence of inerter on natural frequencies of vibration systems." *Journal of Sound and Vibration*, 333 (7): 1874–1887. https://doi.org/10.1016/j.jsv.2013.11.025.

Di Egidio, A., S. Pagliaro, and C. Fabrizio. 2021. "Combined Use of Rocking Walls and Inerters to Improve the Seismic Response of Frame Structures." *J. Eng. Mech.*, 147 (5): 04021016. https://doi.org/10.1061/(ASCE)EM.1943-7889.0001920.

Dong, X., J. Xi, P. Chen, and W. Li. 2018. "Magneto-rheological variable inertia flywheel." *Smart Mater. Struct.*, 27 (11): 115015. https://doi.org/10.1088/1361-665X/aad42b.

Frank Pai, P. 2010. "Online tracking of instantaneous frequency and amplitude of dynamical system response." *Mechanical Systems and Signal Processing*, 24 (4): 1007–1024. https://doi.org/10.1016/j.ymssp.2009.07.014.

Giaralis, A., and F. Petrini. 2017. "Wind-Induced Vibration Mitigation in Tall Buildings Using the Tuned Mass-Damper-Inerter." *J. Struct. Eng.*, 143 (9): 04017127. https://doi.org/10.1061/(ASCE)ST.1943-541X.0001863.

Huang, N. E., Z. Wu, S. R. Long, K. C. Arnold, X. Chen, and K. Blank. 2009. "ON INSTANTANEOUS FREQUENCY." *Adv. Adapt. Data Anal.*, 01 (02): 177–229. https://doi.org/10.1142/S1793536909000096.

Huang, Z., X. Hua, Z. Chen, and H. Niu. 2019. "Performance evaluation of inerter-based damping devices for structural vibration control of stay cables." *Smart Structures and Systems*, 23 (6): 615–626. https://doi.org/10.12989/SSS.2019.23.6.615.

Hwang, J.-S., J. Kim, and Y.-M. Kim. 2007. "Rotational inertia dampers with toggle bracing for vibration control of a building structure." *Engineering Structures*, 29 (6): 1201–1208. https://doi.org/10.1016/j.engstruct.2006.08.005.

Jangid, R. S. 2022. "Optimum parameters and performance of tuned mass damper-inerter for base-isolated structures." *Smart Structures and Systems*, 29 (4): 549–560. https://doi.org/10.12989/SSS.2022.29.4.549.

Jauch, C. 2015. "A flywheel in a wind turbine rotor for inertia control." *Wind Energ.*, 18 (9): 1645–1656. https://doi.org/10.1002/we.1784.

Javidialesaadi, A., and N. E. Wierschem. 2019. "Energy transfer and passive control of single-degree-of-freedom structures using a one-directional rotational inertia viscous damper." *Engineering Structures*, 196: 109339.

https://doi.org/10.1016/j.engstruct.2019.109339.

Kushwaha, P., S. K. Ghoshal, and K. Dasgupta. 2020. "Dynamic analysis of a hydraulic motor drive with variable inertia flywheel." *Proceedings of the Institution of Mechanical Engineers, Part I: Journal of Systems and Control Engineering*, 234 (6): 734–747. https://doi.org/10.1177/0959651819875914.

Li, Q., X. Li, J. Mi, B. Jiang, S. Chen, and L. Zuo. 2021a. "Tunable Wave Energy Converter Using Variable Inertia Flywheel." *IEEE Trans. Sustain. Energy*, 12 (2): 1265–1274. https://doi.org/10.1109/TSTE.2020.3041664.

Li, W., X. Dong, J. Yu, J. Xi, and C. Pan. 2021b. "Vibration control of vehicle suspension with magneto-rheological variable damping and inertia." *Journal of Intelligent Material Systems and Structures*, 1045389X2098388. https://doi.org/10.1177/1045389X20983885.

Ma, R., K. Bi, and H. Zuo. 2023. "An Adaptive Tuned Heave Plate (ATHP) for suppressing heave motion of floating platforms." *Smart Structures and Systems*, 31 (3): 283–299. https://doi.org/10.12989/SSS.2023.31.3.283.

Mahato, A. C., S. K. Ghoshal, and A. K. Samantaray. 2019. "Influence of variable inertia flywheel and soft switching on a power hydraulic system." *SN Appl. Sci.*, 1 (6): 605. https://doi.org/10.1007/s42452-019-0623-0.

Makris, N., and G. Kampas. 2016. "Seismic Protection of Structures with Supplemental Rotational Inertia." *J. Eng. Mech.*, 142 (11): 04016089. https://doi.org/10.1061/(ASCE)EM.1943-7889.0001152.

Makris, N., and G. Moghimi. 2019. "Displacements and Forces in Structures with Inerters when Subjected to Earthquakes." *J. Struct. Eng.*, 145 (2): 04018260. https://doi.org/10.1061/(ASCE)ST.1943-541X.0002267.

Málaga-Chuquitaype, C., C. Menendez-Vicente, and R. Thiers-Moggia. 2019. "Experimental and numerical assessment of the seismic response of steel structures with clutched inerters." *Soil Dynamics and Earthquake Engineering*, 121: 200–211. https://doi.org/10.1016/j.soildyn.2019.03.016.

Marian, Laurentiu, and Giaralis, Agathoklis. 2017. "The tuned mass-damper-inerter for harmonic vibrations suppression, attached mass reduction, and energy harvesting." *Smart Structures and Systems*, 19 (6): 665–678. https://doi.org/10.12989/SSS.2017.19.6.665.

MathWorks. 2022a. "MATLAB: Mathematics (R2022a)." Accessed August 15, 2022. https://www.mathworks.com/help/pdf_doc/matlab/matlab_math.pdf.

MathWorks. 2022b. "Signal Processing Toolbox: User's Guide (R2022a)." Accessed August 15, 2022. https://www.mathworks.com/help/pdf_doc/signal/signal.pdf.

Moaveni, B., and E. Asgarieh. 2012. "Deterministic-stochastic subspace identification method for identification of nonlinear structures as time-varying linear systems." *Mechanical Systems and Signal Processing*, 31: 40–55. https://doi.org/10.1016/j.ymssp.2012.03.004.

Moraes, F. de H., M. Silveira, and P. J. P. Gonçalves. 2018. "On the dynamics of a vibration isolator with geometrically nonlinear inerter." *Nonlinear Dyn*, 93 (3): 1325–1340. https://doi.org/10.1007/s11071-018-4262-6.

Nakamura, Y., A. Fukukita, K. Tamura, I. Yamazaki, T. Matsuoka, K. Hiramoto, and K. Sunakoda. 2014. "Seismic response control using electromagnetic inertial mass dampers: Seismic response control using EIMD." *Earthquake Engng Struct. Dyn.*, 43 (4): 507–527. https://doi.org/10.1002/eqe.2355.

Nayfeh, A. H., and D. T. Mook. 2008. *Nonlinear Oscillations*. John Wiley & Sons.

Smith, M. C. 2002. "Synthesis of mechanical networks: the inerter." *IEEE Trans. Automat. Contr.*, 47 (10): 1648–1662. https://doi.org/10.1109/TAC.2002.803532.

Smith, M. C. 2008. "FORCE-CONTROLLING MECHANICAL DEVICE."

Smith, M. C. 2012. "Force-Controlling Hydraulic Device."

Swift, S. J., M. C. Smith, A. R. Glover, C. Papageorgiou, B. Gartner, and N. E. Houghton. 2013. "Design and modelling of a fluid inerter." *International Journal of Control*, 86 (11): 2035–2051. https://doi.org/10.1080/00207179.2013.842263.

Talley, P. C., A. T. Sarkar, N. E. Wierschem, and M. D. Denavit. 2023. "Performance of structures with clutch inerter dampers subjected to seismic excitation." *Bull Earthquake Eng*, 21 (3): 1577–1598. https://doi.org/10.1007/s10518-022-01514-9.

Ullman, D. G. 1978. "A variable inertia flywheel as an energy storage system." The Ohio State University.

Wang, M., and F. Sun. 2018. "Displacement reduction effect and simplified evaluation method for SDOF systems using a clutching inerter damper." *Earthquake Engng Struct Dyn*, 47 (7): 1651–1672. https://doi.org/10.1002/eqe.3034.

Wang, P., and J. Gao. 2013. "Extraction of instantaneous frequency from seismic data via the generalized Morse wavelets." *Journal of Applied Geophysics*, 93: 83–92. https://doi.org/10.1016/j.jappgeo.2013.04.003.

Wang, Z. H., Y. W. Xu, H. Gao, Z. Q. Chen, K. Xu, and S. B. Zhao. 2019. "Vibration control of a stay cable with a rotary electromagnetic inertial mass damper." *Smart Structures and Systems*, 23 (6): 627–639. https://doi.org/10.12989/SSS.2019.23.6.627.

Xu, T., M. Liang, C. Li, and S. Yang. 2015. "Design and analysis of a shock absorber with variable moment of inertia for passive vehicle suspensions." *Journal of Sound and Vibration*, 355: 66–85. https://doi.org/10.1016/j.jsv.2015.05.035.

Yang, J., J. Z. Jiang, and S. A. Neild. 2020. "Dynamic analysis and performance evaluation of nonlinear inerter-based vibration isolators." *Nonlinear Dyn*, 99 (3): 1823–1839. https://doi.org/10.1007/s11071-019-05391-x.

Yang, S., N. Baddour, and C. Li. 2019. "Design and evaluation of a passive inertial mass device for car suspension system." 80 (1): 18.

Yang, S., T. Xu, C. Li, M. Liang, and N. Baddour. 2016. "Design, Modeling and Testing of a Two-Terminal Mass Device With a Variable Inertia Flywheel." *Journal of Mechanical Design*, 138 (9): 095001. https://doi.org/10.1115/1.4034174.

Yuan, L.-G., F.-M. Zeng, and G.-X. Xing. 2010. "Research on the Design and Control Strategy of Variable Inertia Flywheel in Diesel Generator Unit under Pulsed Load." *2010 International Conference on Computing, Control and Industrial Engineering*, 187–189. Wuhan, China: IEEE.

Zhang, Y., X. Zhang, T. Qian, and R. Hu. 2020. "Modeling and simulation of a passive variable inertia flywheel for diesel generator." *Energy Reports*, 6: 58–68. https://doi.org/10.1016/j.egyr.2020.01.001.

Zhao, Z., R. Zhang, Y. Jiang, and C. Pan. 2019. "Seismic response mitigation of structures with a friction pendulum inerter system." *Engineering Structures*, 193: 110–120. https://doi.org/10.1016/j.engstruct.2019.05.024.